Bedload transport and deposition of mud-grade sediments in deep-lacustrine settings: A case study in the Triassic Yanchang Formation, Ordos Basin, China

YINGCHANG CAO*, MIRUO LIN*, KELAI XI* (iD), SHANG XU* and CAINENG ZOU†
**Key Laboratory of Deep Oil and Gas, China University of Petroleum (East China), Qingdao 266580, China (E-mail: caoych@upc.edu.cn) (E-mail: xikelai@upc.edu.cn)*
†*Research Institute of Petroleum Exploration and Development, PetroChina, Beijing 100083, China*

ABSTRACT

With ongoing shale oil and gas exploration and development across the world, the sedimentology of deep-water fine-grained sedimentary rocks remains an important focus for research. In deep-lacustrine settings, in particular, mud-grade sediments are distributed widely. However, the very fine particle size of mud-grade sediments limits the clear identification of micro-sedimentary structure; the mud-grade sediments are in most facies models believed to be deposited via suspension settling in deep-lacustrine settings. In this study, thin-section observations, advanced mineral identification and characterization system analyses, scanning electron microscopy observations and three-dimensional reconstruction analysis by a focused ion beam-electron beam dual-beam system were conducted on deep-lacustrine mud-grade sediments of the Chang 7_3 sub-member of Triassic Yanchang Formation in the Ordos Basin. Through this multi-proxy approach, evidence of bedload transport of the mud-grade sediments in the deep-lacustrine settings is provided. During the deposition of deep-lacustrine sediments, a significant amount of volcanic material within the mud-grade sediments provided large quantities of high-valence metal cations into the lake waters, which promoted the formation of flocs through electrostatic forces. Subsequently, these flocs are transported as bedload and deposited on the substrate, forming numerous floccule ripples in the deep-lacustrine settings. When floccule ripples form, the flocs continuously pass over the ripple crests under the action of underflow and accumulate downward along the sloping surface of the floccule ripples, developing multiple foresets. Lateral migration and frontal progradation of foresets results in multiple stacked and laterally-connected foresets, ultimately controlling the accumulation and preservation sites of these deep-lacustrine mud-grade sediments. The discovery of floccule ripples and foresets confirms a dynamic deep-lacustrine setting, in which the mud-grade particles can be transported as bedload under the action of underflow and then deposited. A new understanding of the sedimentary process of deep-lacustrine mud-grade particles provides a theoretical basis for clarifying the distribution of mineral composition and organic matter content in mud-grade sediments. It further supports the prediction of favourable shale oil/gas reservoirs, promoting the efficient exploration and development of shale oil and gas resources, globally.

Keywords Bedload transport, deep-lacustrine setting, flocculation, mud-grade sediments, Ordos Basin, sedimentation.

INTRODUCTION

Fine-grained deposits are mud-grade and silt-grade sediments with particle sizes smaller than 0.0625 mm (Aplin & Macquaker, 2011), which account for two-thirds of the global sedimentary rock record and often have a wide distribution in deep-water areas (Peng, 2021). Researchers have mainly focused on the ability of fine-grained sedimentary rocks, particularly mudstones, to act as suitable source rocks for hydrocarbons, whilst paying less attention to the details of sedimentary processes (Schieber, 1991; Könitzer *et al.*, 2014; Peng, 2021). With the continuous progress in shale oil and gas exploration and development, the formation mechanisms of deep-water fine-grained sedimentary rocks remains a focus of research (Loucks & Ruppel, 2007; Jiang *et al.*, 2013; Boulesteix *et al.*, 2019; Zhu *et al.*, 2022; Hou *et al.*, 2023). The composition, character and sedimentary structures within deep-water fine-grained sediments is the foundation and key to studying their formational mechanisms (Mángano *et al.*, 1994; O'Brien, 1996; Schieber *et al.*, 2007).

According to the Udden-Wentworth classification standard (Zhu *et al.*, 2008; Jiang *et al.*, 2013), sediments with particle sizes <0.0039 mm and between 0.0039 and 0.0625 mm are defined as mud-grade and silt-grade, respectively. However, in the Chinese petroleum industry, a decimal classification standard is often used, and sediments with particle sizes less than 0.0100 mm are defined as mud-grade sediments (Zhu *et al.*, 2008). Therefore, in this study, fine-grained sediments with particle sizes less than 0.0100 mm and between 0.0100 and 0.0625 mm are defined as mud-grade and silt-grade sediments, respectively. Typical sedimentary structures, such as graded bedding, erosion surfaces and cross-lamination, in the silt-grade sediments can be characterized by the naked eye and by optical microscopes (Macquaker *et al.*, 2010; Wilson & Schieber, 2014; Boulesteix *et al.*, 2019; Dou *et al.*, 2019). Therefore, research into the observed sedimentary character and associated sedimentation processes of the silt-grade sediments are relatively mature (Bourget *et al.*, 2010; Macquaker *et al.*, 2010; Tombo *et al.*, 2015). Based on the identification of sedimentary structures, silt-grade sediments are often considered to be the deposits of turbidity currents, debris flows, transitional flows or hyperpycnal flows (Stow & Shanmugam, 1980; Boulesteix *et al.*, 2019, 2020; DeReuil & Birgenheier, 2019; Peng, 2021).

However, the particle sizes of mud-grade sediments are finer than those of silt-grade sediments. This makes it difficult to clearly identify the particle structure and micro-sedimentary structure only by the naked eye and the optical microscopes, resulting in a relatively weak study of the sedimentary origin of mud-grade sediments.

In deep-lacustrine settings, mud-grade sediments tend to be more dominant than the coarser-grained sediments and are often widely distributed (Stow & Piper, 1984). Study on the sedimentary origin of mud-grade sediments has also much to offer in terms of understanding of the evolution of sedimentary environments, and will help to further clarify the origin of shale laminae and the associated mechanisms of organic matter enrichment in deep-lacustrine settings (Burton *et al.*, 2014; Ayranci *et al.*, 2018; Boulesteix *et al.*, 2020). At present, the current paradigm suggests that mud-grade sediments are usually formed by the suspension settling of mud-grade particles within a still-water environment of deep-water areas (in this case a lake) (Alçiçek *et al.*, 2007; Aplin & Macquaker, 2011; Tänavsuu-Milkeviciene & Frederick Sarg, 2012; Liang *et al.*, 2018; Wang *et al.*, 2021). However, this single sedimentary process does not fully explain the origin of sedimentary structures recorded in fine-grained rocks observed in deep-water sedimentary basins. For example, weak cross-bedding can be identified from the deep-water mudstones deposited within the Permian Lucaogou Formation in the Jimusar sag, Junggar Basin (Zou *et al.*, 2022). In addition, graded bedding can also be identified in the deep-water mudstones of the Permian Karoo Basin in South Africa (Boulesteix *et al.*, 2022).

Schieber *et al.* (2007) conducted flume experiments and found that muds can be transported and deposited in high-energy sedimentary environments, in a similar way to coarse sediments (Schieber *et al.*, 2007; Schieber & Southard, 2009; Schieber, 2011). In addition, through flume experiments, Baas *et al.* (2011, 2016) confirmed that muds can also deposit in upper transitional plug flow (UTPF) and quasi-laminar plug flow (QLPF); in particular in UTPF, the cross-bedding can be easily identified in the mud deposits (Baas *et al.*, 2016). These findings indicated that, in addition to suspension settling, muds may also undergo transport and deposition through other sedimentation processes. Therefore, through detailed sedimentological and petrological analysis, this study explores insights into the processes

that contribute to the deposition of mud-grade sediments in deep-lacustrine settings.

The Chang 7_3 sub-member of the Triassic Yanchang Formation in the Ordos Basin is a typical area for shale oil exploration and development, and has yielded abundant drilling cores composed of fine-grained sedimentary rocks (Fu *et al.*, 2020; Li *et al.*, 2021a,b), providing favourable conditions for studying the sedimentary processes of deep-water fine-grained sediments. This study focuses on the mud-grade sediments and addresses the following two specific scientific questions: (i) how to clearly characterize the micro-sedimentary structures in deep-lake mud-grade sediments; (ii) what is the sedimentary process of mud-grade particles in deep-lacustrine settings? The research results can help improve understanding of the sedimentary origin of mud-grade sediments, specifically in deep-lacustrine settings. According the sedimentary origin and spatial distribution of mud-grade sediments, the changes of their mineral compositions and organic matter contents in different positions of the basin can be predicted. Rock composition plays an important role in controlling the reservoir properties and oiliness of shale oil and gas reservoirs (Jin *et al.*, 2021). Therefore, the research results are also helpful for the selection of favourable shale oil/gas reservoirs, which will further promote the efficient exploration and development of shale oil and gas resources, globally.

GEOLOGICAL BACKGROUND

The Ordos Basin is a large multi-cycle cratonic basin located in the western North China Block. It is bound to the east by Lvliang Mountain and the Lishi Fault, to the west by Helan Mountain, to the north by the Xing'an Mongolian Orogenic Belt and the Dengkou-tuoketuo Fault, and to the south by the Qinling Orogenic Belt and Huaibei Flexure Belt (Fig. 1).

During the accumulation of the Triassic Yanchang Formation, a large-scale inland-depression lake basin formed. During this period, a set of terrigenous clastic rocks, mainly composed of fluvial–lacustrine and lacustrine facies, were deposited in the basin. These deposits are subdivided into ten members, termed Chang 10 to 1 from base to top, which record the complete sedimentary record of the formation, including inception, development, peak and final fill stages of a lacustrine basin (Zhang *et al.*, 2021a,b). During the accumulation of the Chang 7 member, the limits of the lacustrine basin retreated and expanded rapidly, leading to the development of organic-rich shales and sandstones of gravity flow origin (Fu *et al.*, 2020). The Chang 7 member can be further divided into three sub-members: Chang 7_1, Chang 7_2 and Chang 7_3. Among them, a relatively warm–humid palaeoclimate and intermittent volcanic activity occurred during the deposition of the Chang 7_3 sub-member. During this period, the lake level increased significantly, and the lake area exceeded 5×10^4 km^2, with a water depth in the deep-lacustrine setting reaching 150 m (Yuan *et al.*, 2015; Fu *et al.*, 2019). The relatively strong hydrodynamics at the edge of the basin resulted in the deposition of sandstones within a deltaic depositional system, the average cumulative thickness of sandstone and siltstone is 24.8 m, while the cumulative thickness of the mudstone and shale is mainly distributed between 5 m and 20 m (Li *et al.*, 2012). However, in the semi-deep and deep-lake locations, the hydrodynamics were relatively weak (Zhang *et al.*, 2016; Wang *et al.*, 2021), allowing the accumulation of thickly-bedded organic-rich shales, and some interbedded gravity flow deposits (sandstones) (Fig. 1B to C). Deep-lacustrine shales are widely distributed in the basin, with an accumulated thickness mainly exceeding 25 m and a maximum thickness of up to 50 m, while the average cumulative thickness of sandstone and siltstone is 7.9 m (Li *et al.*, 2012; Liu *et al.*, 2014, 2021). With the increasing exploration and development of shale oil in the Ordos Basin, multiple wells in the deep-lacustrine setting have obtained continuous core data from the Chang 7_3 sub-member (Fu *et al.*, 2018), which provides extremely favourable conditions for studying the sedimentation of deep-water mud-grade sediments.

MATERIALS AND METHODS

Five boreholes (Wells Ch96, N70, C30, Z282 and N228) with core through the Chang 7_3 sub-member were selected from the Ordos Basin. The lengths of continuous coring are 40 m in Well Ch96, 35.3 m in Well N70, 23 m in Well C30, 11.4 m in Well Z282 and 32 m in Well N228. Four typical samples, with clear and relatively flat laminae interfaces, were selected for advanced mineral identification and characterization system (AMICS) analyses, and 102 samples were selected for thin-section petrographical
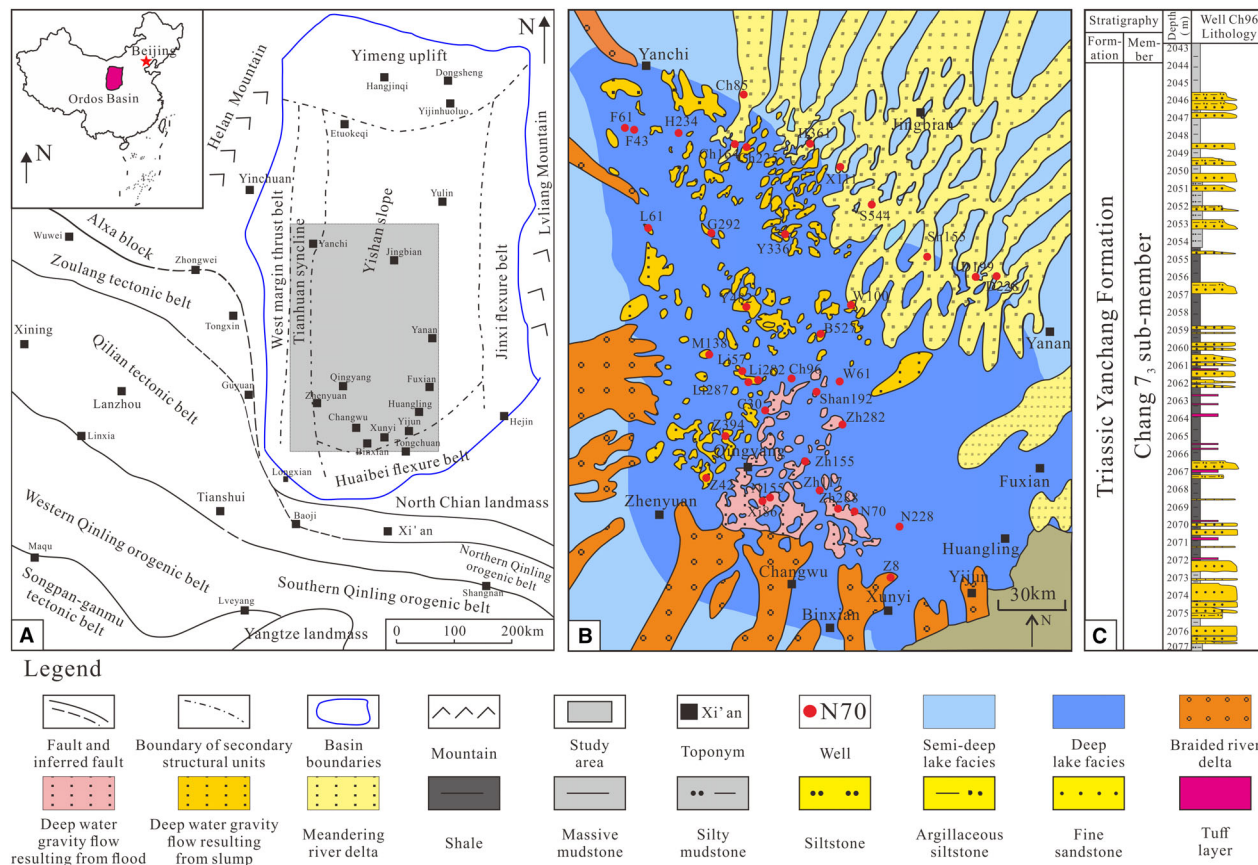
Fig. 1. Map showing the location of the study area, the distribution of sedimentary facies and the stratigraphy of the study area: (A) tectonic setting of the Ordos Basin showing the location of uplifts, flexure belts and orogenic belts (Zhou *et al.*, 1995); (B) plane view showing the distribution of sedimentary facies and studied wells from the Chang 7$_3$ sub-member; (C) stratigraphic column of the Chang 7$_3$ sub-member.

analysis. Subsequently, *in situ* laser ablation – inductively coupled plasma – mass spectrometry (LA-ICP-MS) analysis was conducted on twenty-one rock samples to determine the geochemical characteristics. A combination of thin-section observations (102 samples were used), scanning electron microscopy (SEM) analysis (five samples were used) and three-dimensional reconstruction analysis by FIB-SEM (focused ion beam – scanning electron microscopy; four samples were used) were performed to characterize the two-dimensional and three-dimensional features of the particle structure and micro-sedimentary structure.

Petrographical analysis focused on the identification of mineral type, particle structure and two-dimensional features of micro-sedimentary structure within the mud-grade sediments, using a Zeiss microscope (Imaging-2M) and a scanning electron microscope (Zeiss Crossbeam 550 FIB-

SEM; Carl Zeiss AG, Oberkochen, Germany). Quantitative statistics of the mineral compositions were calculated using AMICS analysis and a scanning electron microscope (Zeiss Crossbeam 550 FIB-SEM) integrated with a Bruker energy-dispersive X-ray spectrometer (EDS; Bruker, Billerica, MA, USA) analysis system (X-Flasher Detector 430-M). For AMICS analysis, thin sections were firstly carbon-coated and glued onto aluminium stubs. The area was then scanned using backscattered electron (BSE) analysis, followed by automatic mineral identification using high-resolution EDS. The AMICS analysis software and the databases of energy spectrum characteristics of different minerals were finally used for identifying mineral boundaries resolvable up to 20 μm. The microscopy, SEM-BSE and AMICS analyses were conducted at the Key Laboratory of Deep Oil and Gas, China University of Petroleum (East China).

The LA-ICP-MS analysis was used to obtain the relative major and trace element content of the mud-grade sediments, which were used for provenance clarification. Laser sampling was performed using GeoLas 2005 (Lambda Physik, Göttingen, Germany). An Agilent 7500a ICP-MS instrument (Agilent Technologies, Santa Clara, CA, USA) was used to acquire ion signal intensities. Agilent ChemStation was utilized for the acquisition of each individual analysis. Helium (as a carrier gas) and argon (as a make-up gas) were mixed via a T-connector prior to the entry of the ICP. One hundred and sixty successive laser pulses (4 Hz) in an area of 44 μm ablated the surface of the sample for about 40 s. Before performing a laser ablation on each sample, monitoring the gas blank for 20 s is required. The element content was calibrated using multiple reference materials (NIST SRM 610, NIST SRM 612, BCR-2G, BIR-1G and BHVO-2G) without applying internal standardization (Liu *et al.*, 2008). After every five samples a standard sample analysis was performed that served as quality control to correct the time-dependent drift of sensitivity and mass discrimination. Test points were carefully selected on each lamina to ensure that the major element content (RSD < 1 to 2%) and trace element content (RSD = 1 to 4%) could be accurately obtained (Liu *et al.*, 2008). Offline processing of analytical data, including the selection of samples and blank signals, instrument sensitivity drift correction and calculation of elemental content, was performed using the software ICPMSDataCal (Liu *et al.*, 2008).

In situ cutting and three-dimensional reconstruction by FIB-SEM were used to reconstruct the three-dimensional characteristics of the particle structure and micro-sedimentary structure. Experiments were conducted using a Zeiss Crossbeam 550 FIB-SEM instrument. Firstly, the surface of the tested sample was subjected to argon ion milling and placed on a sample stage. The sample stage was rotated by 54°, and the electron and ion beams were focused. A gallium ion beam with a beam current of 65 nA and an energy of 30 kV was used to dig a trapezoidal groove underneath the selected area. Ear grooves were dug on both sides of the selected area using a beam current of 30 nA and an energy of 30 kV. Finally, a finely polished ion beam with a beam current of less than 30 nA was used to precisely polish the cross-section of the selected area. During sample sectioning, continuous slicing of the selected area was performed at 70 nm

intervals using an ion beam of 30 kV and 7 nA. During the cutting process, imaging was performed using an electron beam at 1 kV and 500 pA. Dragonfly Pro software (Zeiss) was used to perform the three-dimensional reconstruction of all sliced images. Pre-processing image alignment and noise reduction were performed. The 'Define range' function was used to select the greyscale value range (based on the composition of mud-grade sediments). Finally, the '3D mode' function was used to extract the mineral regions; this operation was repeated to extract the mineral regions that are separated by organic matter. The mineral regions were then displayed together and overlapped, which provided the final three-dimensional characteristic model of the particle structure and micro-sedimentary structure.

Gamma logging data and machine learning were used to identify the distribution of mud-grade sediments in deep-lacustrine settings. The gamma values of deep-lacustrine shale rich in radioactive uranium are typically higher than those of massive mudstone and sandstone (Yang *et al.*, 2016; Zhao *et al.*, 2020). In general, the gamma value of the mudstone is between 120 API and 180 API, while the gamma value of the shale is much higher than 180 API (Yang *et al.*, 2016). Therefore, the authors can first identify the locations of the shale intervals in each well using gamma logging data. In addition to the difference in gamma values, there are also significant differences in mineral composition among deep-lacustrine shale, massive mudstone and sandstone (Liu *et al.*, 2021; Lin *et al.*, 2024). The X-ray diffraction (XRD) data shows that the contents of quartz and feldspar in deep-lacustrine shales are in the range of 15.3 to 28.0% and 4.1 to 9.5%, respectively (Lin *et al.*, 2024). The contents of clay minerals can reach up to 55% and the clay minerals are from 13.0 to 33.1% (Lin *et al.*, 2024). In contrast, the quartz and feldspar in massive mudstones range from 39.9 to 47.4% and 4.8 to 11.4% in content (Lin *et al.*, 2024), while the content of organic matter can only reach 5.8% (Lin *et al.*, 2024). The total contents of quartz and feldspar in sandstones is significantly more than 80% (Lin *et al.*, 2024). Therefore, given the mineralogical differences among shale, mudstone and sandstone (Liu *et al.*, 2021), it is possible to clarify the distribution of different rock types within the Ordos Basin on the basis of machine learning. In order to continuously identify the mineral content in the vertical direction, the

main mineral types in the research area and well log data that are sensitive to changes in mineral components were sorted and taken as the predicted objective values and input parameters, respectively (Zhang *et al.*, 2021b). The mineral content was provided by XRD data. Logging data with higher correlation indices with the mineral contents were selected as the main controlling factors to identify the mineral content, which can reduce complexity and enhance accuracy of the model (Zhang *et al.*, 2021b). After that, the sensitive logging data and corresponding mineral content were imported into the training dataset and training of machine learning was started. The model of machine learning was constructed by using Tensorflow online open source code software library (Zhang *et al.*, 2021b). The program for machine learning was written by Python 3.0 design language, machine learning was used to quantitatively predict individual minerals, and Keras was adopted to build, evaluate and supervise the machine learning model. The detailed training process is discussed in Zhang *et al.* (2021b)). Finally the machine learning model generated the mathematical expressions that were used to continuously identify the mineral content in the vertical direction in each well.

RESULTS

Lithofacies analysis for the fine-grained sedimentary rocks in the deep-lacustrine setting

Based on the core observation and thin-section analysis, four lithofacies can be identified in the fine-grained sedimentary rocks of the Chang 7_3 sub-member within the Ordos Basin (Table 1). The laminated shales of large thickness are widely distributed in the deep-lacustrine setting, while the sandstones and siltstones are deposited as thin interlayers, and the massive mudstones can occur interbedded with sandstones/siltstones. In this study, the foresets can be commonly identified in the laminated shales enriched in clay minerals. This seems to imply that the mud-grade sediments are not only deposited in a continuous still water environment. In order to emphasize that this paper mainly discusses the sedimentary origin of mud-grade sediments with foresets in deep water area, 'laminated shale' is referred to as 'deep-lacustrine mud-grade sediments' in the following content of this article.

Composition of the deep-lacustrine mud-grade sediments

Mineral composition

Compared with other inorganic minerals, the clay mineral content is relatively high in the fine-grained sedimentary rocks of the Chang 7_3 sub-member (Fig. 2A). The organic matter content can reach 14.44%, which often shows a layered distribution (Fig. 2A). Layered organic matter and clay minerals typically alternate vertically (Fig. 2A). Frequent changes in organic matter content led to the formation of laminated features in the fine-grained sedimentary rocks, inducing shale deposition in the deep-lacustrine setting (Fig. 2A). At the position with relatively low organic matter (LOM) content, the mixed layers of illite/smectite reach nearly 80% by volume, with a small amount of pyrite; the content of plagioclase and quartz is 1.70% and 2.60%, respectively, and the volume content of organic matter is 5.13% (Fig. 2B). At the position with relatively high content of organic matter (HOM), the mixed layers of illite/smectite reach nearly 72% by volume, and the volume content of organic matter and pyrite can reach 14.44% and 8.5%, respectively (Fig. 2C). The pyrite is commonly observed in association with higher levels of organic matter. The feldspar and quartz content is relatively low, at 0.82% and 2.81%, respectively (Fig. 2C).

Geochemical characteristics

In situ analyses of major and trace elements was conducted on the mud-grade sediments. After normalization to the Australian Palaeozoic shale (PAAS – the provenance is a typical highly mature terrigenous clasts) and chondrite, spider diagrams of major and trace elements (Fig. 3A and B) and patterns of rare earth elements (REE) (Fig. 3C) were established. The results indicate that the variation in organic matter content did not significantly affect the distribution of major and trace elements or REE patterns, suggesting that the provenance of these mud-grade sediments was relatively consistent throughout their deposition. Overall, compared to the PAAS, the mud-grade sediments of the Chang 7_3 sub-member are richer in high-valence metal cations, such as Fe, V, Cu, Pa and U (Fig. 3A and B). The $(La/Yb)_N$ ratios were mainly distributed between 4.00 and 13.80, showing the characteristics of light REE enrichment (Taylor & McLennan, 1995) (Fig. 3C). The distribution ranges of Zr/TiO_2 and Nb/Y ratios range

Table 1. Lithofacies scheme of the fine-grained sedimentary rocks in deep-lacustrine setting of the Ordos Basin.

Facies code	Facies title	Thickness range (m)	Sedimentary structure	Description
F1	Laminated shale	0.15–10.00	Floccule ripple, foreset	Laminated shales usually appear dark black and are widely distributed in the deep-lacustrine setting. Clay mineral and organic matter are typically rich in F1, which can reach up to 55.0% and 33.1%, respectively. Floccule ripples and foresets can generally be identified in F1, implying that the clay minerals may not only occur as suspension settling in the deep-lacustrine setting. F1 are mainly sourced by volcaniclastic materials from Qinling orogenic belts (Lin *et al.*, 2024), which is an important reason for the enrichment of radioactive uranium in F1 (Zhao *et al.*, 2020)
F2	Structureless mudstone	0.17–7.22	Structureless	Structureless mudstones are black grey and they are usually interbedded with sandstones/siltstones; the deformation structure is occasionally identified in F2; the provenance of F2 is mainly from the Archaean–Palaeozoic parent rocks (Zhang *et al.*, 2013)
F3	Sandstone	0.07–2.62	Structureless, parallel bedding, normally graded bedding, inversely graded bedding	Sandstones are light grey and occasionally contain deformation structures; the floating mud-clasts can be commonly identified in the structureless sandstone with sharp contacts at base and top; the erosional bases and load casts are present at the bottom of normally-graded sandstones; the inversely-graded sandstones usually develop in the lower part of normally-graded sandstone forming inverse then normal graded rhythmic successions; the provenance of F3 is mainly from the Archaean–Palaeozoic parent rocks (Lin *et al.*, 2024)
F4	Structureless siltstone	0.10–2.28	Structureless	Structureless siltstones contain floating mud-clasts, and the contacts at the base and top boundary of F4 are sharp; the deformation structure can be occasionally identified in F4; the provenance of F4 is mainly from the Archaean–Palaeozoic parent rocks (Lin *et al.*, 2024)

between 0.01 to 0.03 and 0.30 to 1.00, respectively, all within the ranges corresponding to those sourced from intermediate-basic volcanic rocks (Fig. 3D). Due to the mud-grade sediments containing a high occurrence of mixed layers of illite/smectite, and their geochemical characteristics being very similar to volcanic rocks, the volcaniclastic materials may be mainly mixed in the mud-grade sediments. Previous study has proved that the volcanic eruptions in Qinling orogenic belts can provide the volcaniclastic materials for the deep-lacustrine shales (Lin *et al.*, 2024). In addition, during deposition of the Chang 7_3 sub-member, the deep-lacustrine area can also receive the sediments from Archaean–Palaeozoic parent rocks in the north-east and south-west
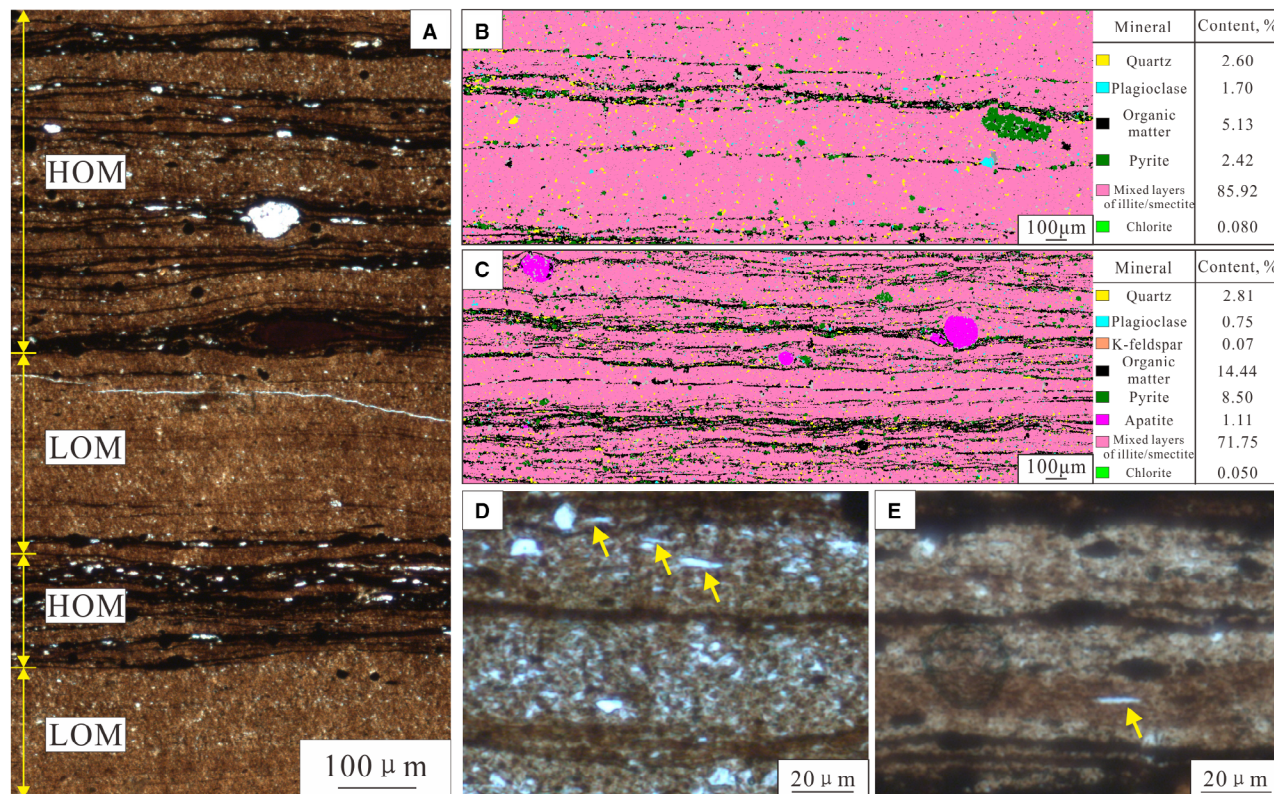
Fig. 2. Mineral composition of the deep-lacustrine mud-grade sediments. (A) Microscopic characteristics of the mud-grade sediments under polarized light, Well Z282, 1791.37 m. (B) The result of advanced mineral identification and characterization system (AMICS) analysis at the position with relatively low organic matter content. (C) The result of AMICS analysis at the position with relatively high organic matter content. (D) Rod-like feldspars with clean surfaces at the LOM under polarized light. (E) A rod-like feldspar with a clean surface at the HOM under polarized light. HOM = Position with relatively high organic matter content; LOM = Position with relatively low organic matter content.

provenances (Wang *et al.*, 2013). The Al_2O_3/TiO_2 can be used to effectively analyse the provenances of fine-grained sediments (Fritz & Vanko, 1992; Hayashi *et al.*, 1997). This study found that the REE patterns, inactive element ratios and the distribution range of Al_2O_3/TiO_2 in mud-grade sediments are very similar to those of andesite in the western Qinling orogenic belts (Fig. 3C and D). These extrusive rocks have been dated as 231.7 ± 2.1 to 226.3 ± 1.1 Ma (Liu *et al.*, 2018; Li *et al.*, 2019), which corresponds with the depositional period of the Chang 7_3 sub-member (Li & Yang, 2023). Therefore, the authors interpreted that the mud-grade sediments mainly derived from the Triassic volcaniclastic deposits from the western Qinling orogenic belts. However, some mud-grade sediments show relatively high and low Al_2O_3/TiO_2, which range from 30.9 to 51.0 and from 18.2 to 20.0 (Fig. 4). This indicates that the

volcaniclastic deposits from southern Qinling orogenic belts and the deposits from Archaean–Palaeozoic parent rocks can also be mixed in the mud-grade sediments (Fig. 4). Therefore, the mud-grade sediments are composed of volcaniclastic and clastic materials, which indicates that the volcaniclastic materials transported into the lake basin by surface runoff rather than falling out of the atmosphere. After a volcanic eruption, volcaniclastic material can settle rapidly on the ground and then weather into smectite through hydrolysis or hydration (Cuadros *et al.*, 1999; Huff, 2016). When the altered volcaniclastic materials enter the lake basin, it can be further transported towards the deep-lacustrine setting by underflows or by buoyant plumes, providing the material basis for the deposition of mud-grade sediments (Plint, 2014; Boulesteix *et al.*, 2019). A large number of high-valence metal cations can be released into lake waters
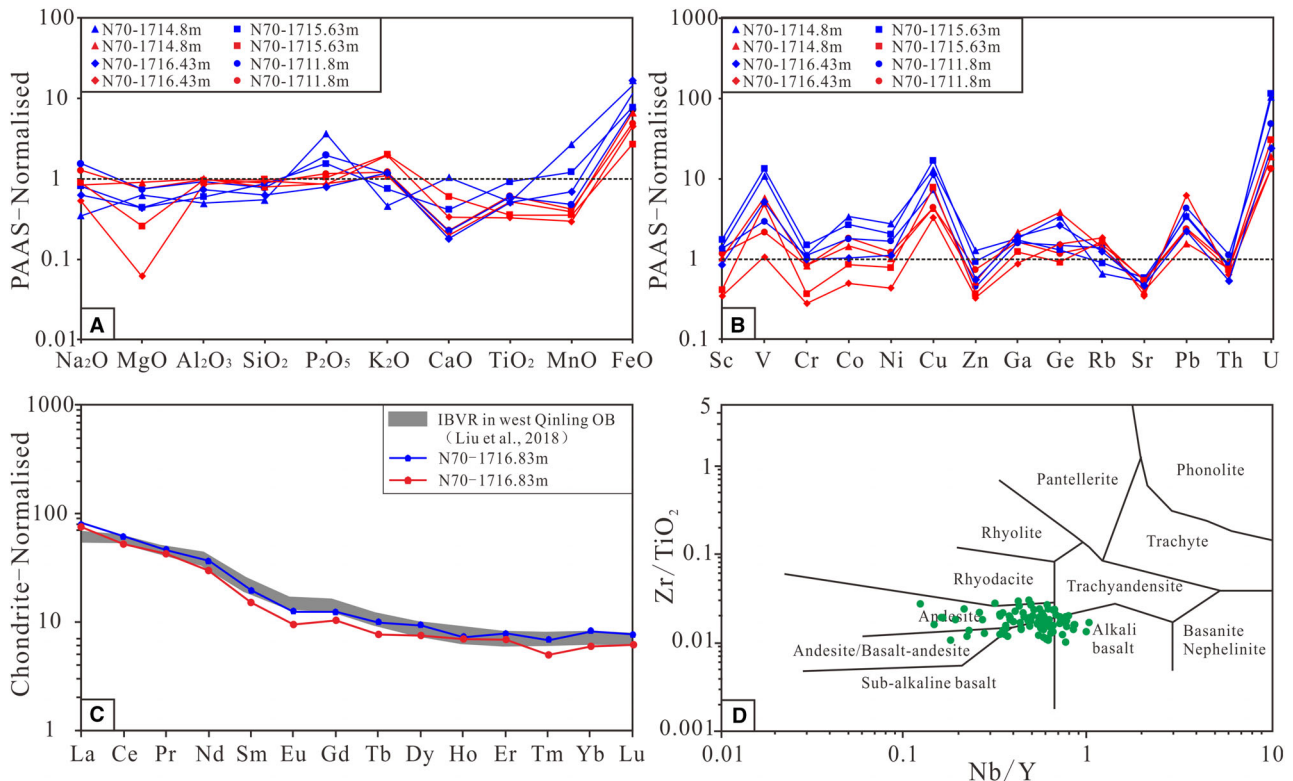
Fig. 3. Geochemical characteristics of the mud-grade sediments. (A) Spider diagram showing the distribution of major elements after standardization of PAAS (Post-Archean Australian Shale). (B) Spider diagram showing the distribution of trace elements after standardization of PAAS. (C) Rare earth element (REE) pattern after standardization of chondrite; the red lines in (A) to (C) represent the geochemical characteristics at the LOM, while the blue lines represent the geochemical characteristics at the HOM; (D) distribution of Zr/TiO_2 and Nb/Y ratios in the mud-grade sediments. The databases of Zr/TiO_2 and Nb/Y ratios were obtained from the twenty-one samples in Well N70. At least two repeated elemental analyses were conducted on each sample to ensure that the test data can represent element enrichment characteristics of each sample. IBVR = Intermediate-basic volcanic rocks; OB = Orogenic belts; HOM = Position with relatively high organic matter content; LOM = Position with relatively low organic matter content.

during these processes (Frogner *et al.*, 2001; Duggen *et al.*, 2007), which may affect the depositional process of mud particles.

Particle structures identified in the mud-grade sediments

Polarizing microscopic observations revealed the presence of scattered feldspar particles within the mud-grade sediments. The feldspar surfaces are clean and form rod-like shapes (Fig. 2D and E). These angular feldspars are randomly distributed, and their long axes are not aligned in an obvious directional orientation (Fig. 2D). The SEM observation reveals that the distribution of clay minerals often lacks apparent directional features in the clay mineral layers (CML) (Fig. 5). Clay minerals mainly exhibit 'edge–face' contacts with one another, as well as partial

'edge–edge' and 'face–face' contacts (Fig. 5C). On this basis, characterization of spatial distribution of the clay minerals and their contact features was further achieved through three-dimensional reconstruction analysis (Fig. 5D). According to the difference of greyscale value between clay and intercrystalline pore, the single crystal morphology of clay minerals can be extracted, and it was found that they are not aligned in an obvious directional orientation (Fig. 5E). One end of a single flake-shaped clay mineral is in contact with the surface of another flake-shaped clay mineral (Fig. 5E and F), presenting a distinct 'edge–face' contact. Multiple flake-shaped clay minerals form cardhouse stacking owing to their mutual 'edge–face' contacts, forming the typical floc structure (Bennett *et al.*, 1991; Wang *et al.*, 2003; Slatt & O'Brien, 2011) (Fig. 5E and F). During burial compaction,
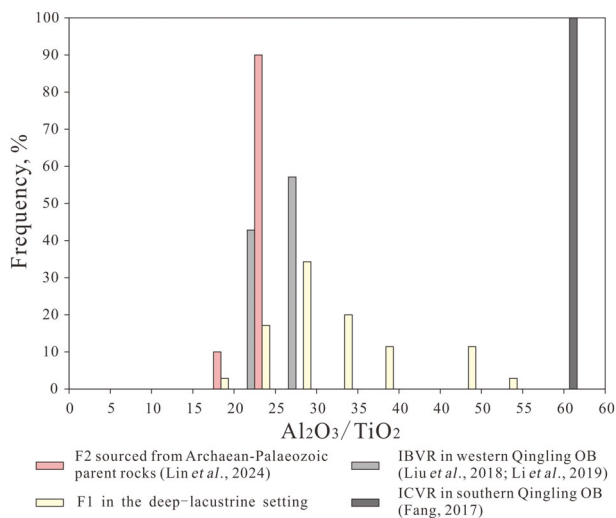
Fig. 4. Frequency distribution map of Al_2O_3/TiO_2 ratios in F1, F2 and the Triassic volcanic rocks from Qinling orogenic belts.

the flocs are subsequently squeezed and deformed, resulting in closer contacts than their original depositional texture (Fig. 6). Because of the similarity in the composition of each floc, the outline of a single floc in fine-grained sedimentary rocks is often difficult to discern (Li *et al.*, 2021a,b); however, in some cases, it is possible to identify the floc structure (Fig. 6F) (Slatt & O'Brien, 2011). The identification of floc structures implies that, in deep-lacustrine settings, the mud-grade particles can be transported and deposited in the form of flocs in addition to the background settling (Fig. 5).

However, based on the SEM observations, the floc structure formed by clays cannot be identified in the organic layers (OL) (Fig. 7). The microscopic observations and AMICS analyses indicate that the clay content within OL is relatively low (Figs 2B, 2C, 7A and 7B), and the single particles of clay minerals have only minimal contact with one another, exhibiting a directional orientation along the direction of laminae (Fig. 7C). Different clay minerals are also distributed parallel to one another (Fig. 7D). It is interpreted that the organic matter and clay within OL were deposited through suspension settling in a still water environment (*sensu* O'Brien *et al.*, 1980; Aplin & Macquaker, 2011). The still water environments significantly reduce the probability of contact between individual clay minerals, which inhibits the formation of a large number of flocs (Aplin & Macquaker, 2011).

Micro-sedimentary structures identified in the mud-grade sediments

Given the fine particle size of the deep-lacustrine mud-grade sediments, any potential sedimentary structures are challenging to visually identify from the core data alone. Therefore, this study uses a combination of both high-resolution microscopic description and three-dimensional reconstruction techniques to identify any micro-sedimentary structures preserved within the mud-grade sediments. Thin-section observations revealed that the foresets are commonly recorded in the CML, but not recognized in the OL (Fig. 8). Each foreset is separated by organic matter, which provides a good identification marker for dividing different foresets.

However, only the local features of sedimentary structures can be observed in the two-dimensional plane, and the characteristics of sedimentary structures perpendicular to this plane cannot be accurately represented. This may lead to the omission of important information on sedimentary structures, which introduces uncertainty in the analysis of the sedimentation of mud-grade sediments. For example, the lenticular fabric and floccule ripples indicate a completely different transport and depositional process for the fine-grained sediments (Schieber *et al.*, 2007, 2010). However, in the cross-sections perpendicular to the lamina, both lenticular fabric and floccule ripples exhibit lenticular features (Schieber *et al.*, 2007, 2010). Therefore, based on the fine characterization of two-dimensional sedimentary structures, a detailed three-dimensional depiction of sedimentary structure is required. In this study, the interface of silty-grained felsic laminae was chosen as the horizontal interface during the period of mud-grade sediment deposition. In order to reconstruct the spatial distribution of each foreset, the position with high organic matter content was selected for *in situ* cutting and three-dimensional reconstruction by FIB-SEM (Fig. 9A and B), and the cutting position was located parallel to the silty-grained felsic laminae. This analysis allowed the identification of eight stages (stages I to VIII) of foresets in the selected area (Fig. 9C). During the deposition of stages I to III, the foresets are successively deposited upon the underlying slope surface (Fig. 9D). In the selected area, the slope surface formed by the earlier deposited foresets was completely covered by the later deposited foresets (Fig. 9D). However, during the deposition of stages IV to VIII, significant changes were observed in the
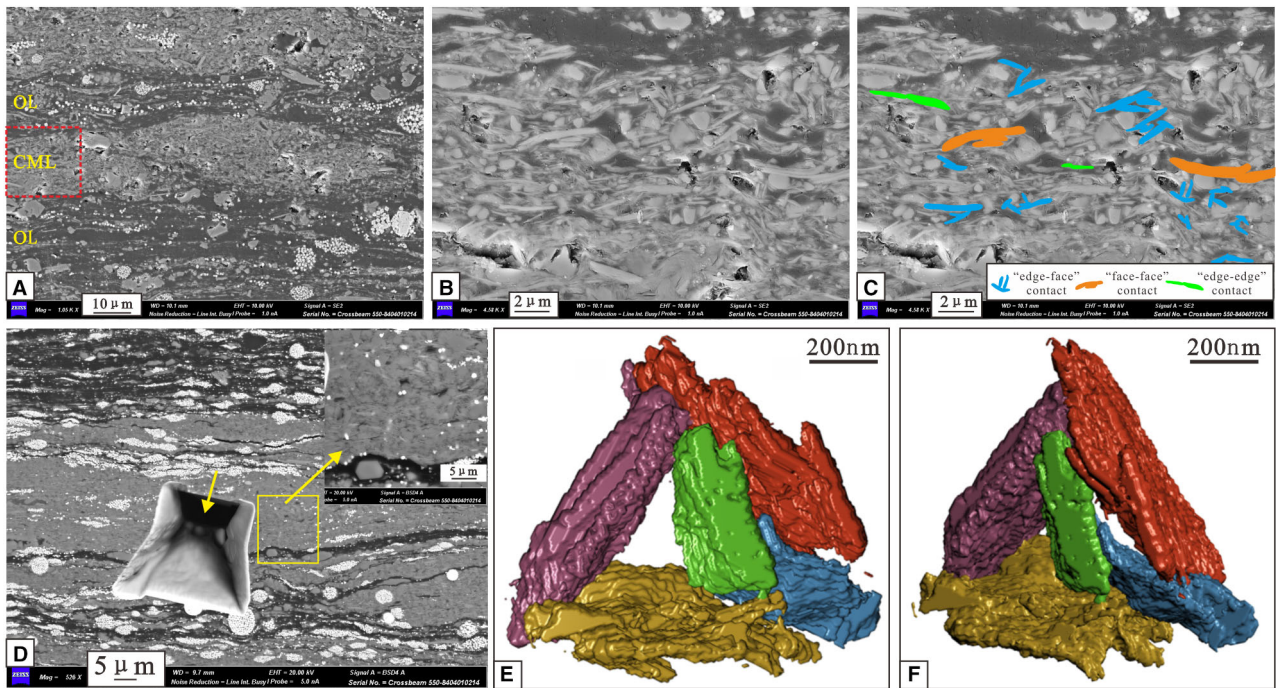
Fig. 5. Floc structure identified in the mud-grade sediments. (A) to (C) Microscopic characteristics of floc structure under SEM analysis, Well C30, 1967.67 m; image (B) shows the microscopic features within the red dashed box in image (A), where the distribution of clay minerals is not aligned in an obvious directional orientation, such as 'edge–face' contact; image (C), taken from the same field of view as image (B), indicates the contact relationship between some of the clay minerals; (D) characteristics of the occurrence of clay minerals in the selected area (yellow solid box) that is cut by a focus ion beam; (E) the result of three-dimensional reconstruction of spatial distribution of clay minerals in the selected area from image (D); (F) the results of *ca* 30° counterclockwise rotation of the image (E). The different coloured bars in images (E) and (F) represent different clay mineral types. CML, clay mineral layer; OL, organic layer.
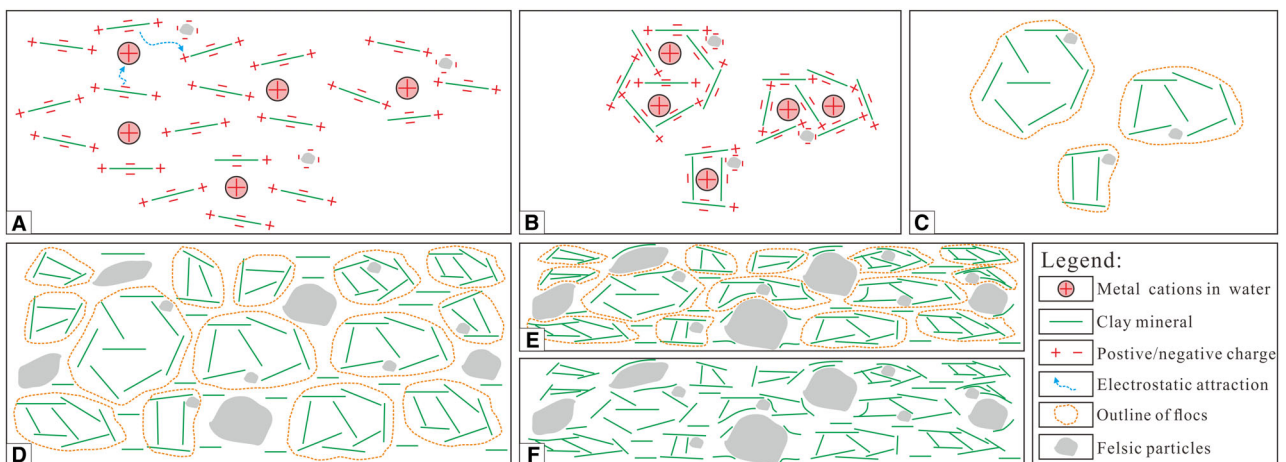
Fig. 6. A possible process of floc formation and their morphological characteristics after burial and compaction. (A) In the presence of metal cations in lake water, the electrostatic force promotes agglomeration between clay and feldspar particles; (B) clay minerals and feldspars agglomerate to form flocs; (C) flocs and their contour characteristics; the formation processes of flocs in the images (A) to (C) were modified from Bennett *et al.* (1991); (D) morphological characteristics and distribution of flocs before burial compaction; (E) morphological characteristics and distribution of flocs after burial compaction (modified from Li *et al.*, 2021a,b); (F) morphological characteristics and distribution of flocs after burial compaction (removing the outline of flocs).

© 2024 International Association of Sedimentologists, *Sedimentology*
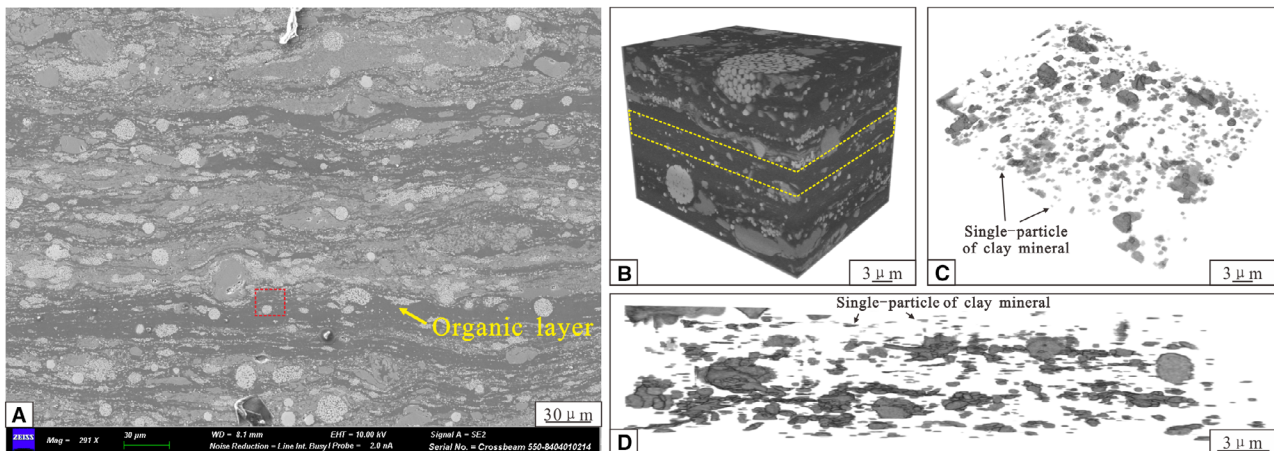
Fig. 7. Distribution of clay minerals in the organic layers of mud-grade sediments. (A) Microscopic characteristics of the organic layers under SEM analysis, Well N228, 1760.75 m. (B) The three-dimensional dataset obtained by cutting-out the area within the red dotted box in image (A). (C) The three-dimensional reconstruction (top view) of inorganic minerals within the yellow dotted box in image (B). (D) The three-dimensional reconstruction (front view) of inorganic minerals within the yellow dotted box in image (B). The clay minerals in the organic layers exhibit directional orientation along the direction of shale laminae.

coverage of the foresets upon the underlying slope surface. That is, from covering a large area on the left side (stage IV, Fig. 9E), to covering the entire underlying slope surface (stage V, Fig. 9F), then covering a few areas on the right side (stage VI, Fig. 9G), and finally covering the entire underlying slope surface (stages VII and VIII, Fig. 9H and I). These phenomena are interpreted as a lateral migration of the mud-grade deposits due to a continuous change in the shape of bedforms.

The development of foresets in the mud-grade sediments requires an uneven bedform as the foundation (Schieber & Yawar, 2009). Microscopic observations show that the foresets commonly deposited above lenticular clay aggregates (Fig. 8). This suggests that deposition of foresets may be facilitated by the presence of lenticular clay aggregates as a necessary basal condition (Schieber et al., 2007; Schieber & Yawar, 2009; Schieber, 2011). Therefore, the lenticular clay aggregates with about 40 μm length were selected to finely reconstruct its three-dimensional characteristics (Fig. 10A and B). The lenticular clay aggregates typically appear as a crescent-shaped form (Fig. 10C). In the cross-sections perpendicular to the shale laminae, the lenticular clay aggregates also display lenticular features (Fig. 10A and B). Therefore, the lenticular clay aggregates are interpreted as the product of floccule ripples that developed

on the substrate (Schieber et al., 2007; Plint, 2019). After the development of floccule ripples, the foresets continuously deposit above the floccule ripples to form the CML (Fig. 10). The identification of floc structure, floccule ripples and foresets within the CML indicates that the transport and deposition of clay minerals in the deep-lacustrine setting are closely related to the action of underflows.

Distribution of mud-grade sediments in deep-lacustrine settings

In the Chang 7_3 sub-member, the deep-lacustrine shales present higher GR values compared with the massive mudstones and sandstones, which is due to the enrichment of radioactive uranium elements (Yang et al., 2016). The enrichment of volcaniclastic deposits within the deep-lacustrine shales is an important reason for their relatively high content of radioactive uranium (Zhao et al., 2020). As for the reference standard of North American Shale Composite (NASC), the contents of thorium (Th), uranium (U) and potassium (K) are 12.3 ppm, 2.66 ppm and 3.20%, respectively, which convert to an equivalent gamma-ray log reading of 121.7 API units (https://www.kgs.ku.edu/PRS/ReadRocks/GRLog.html). Compared to the reference standard, the values of Th and K within the deep-lake shales are 16.74 ppm and 2.61%, while the content of
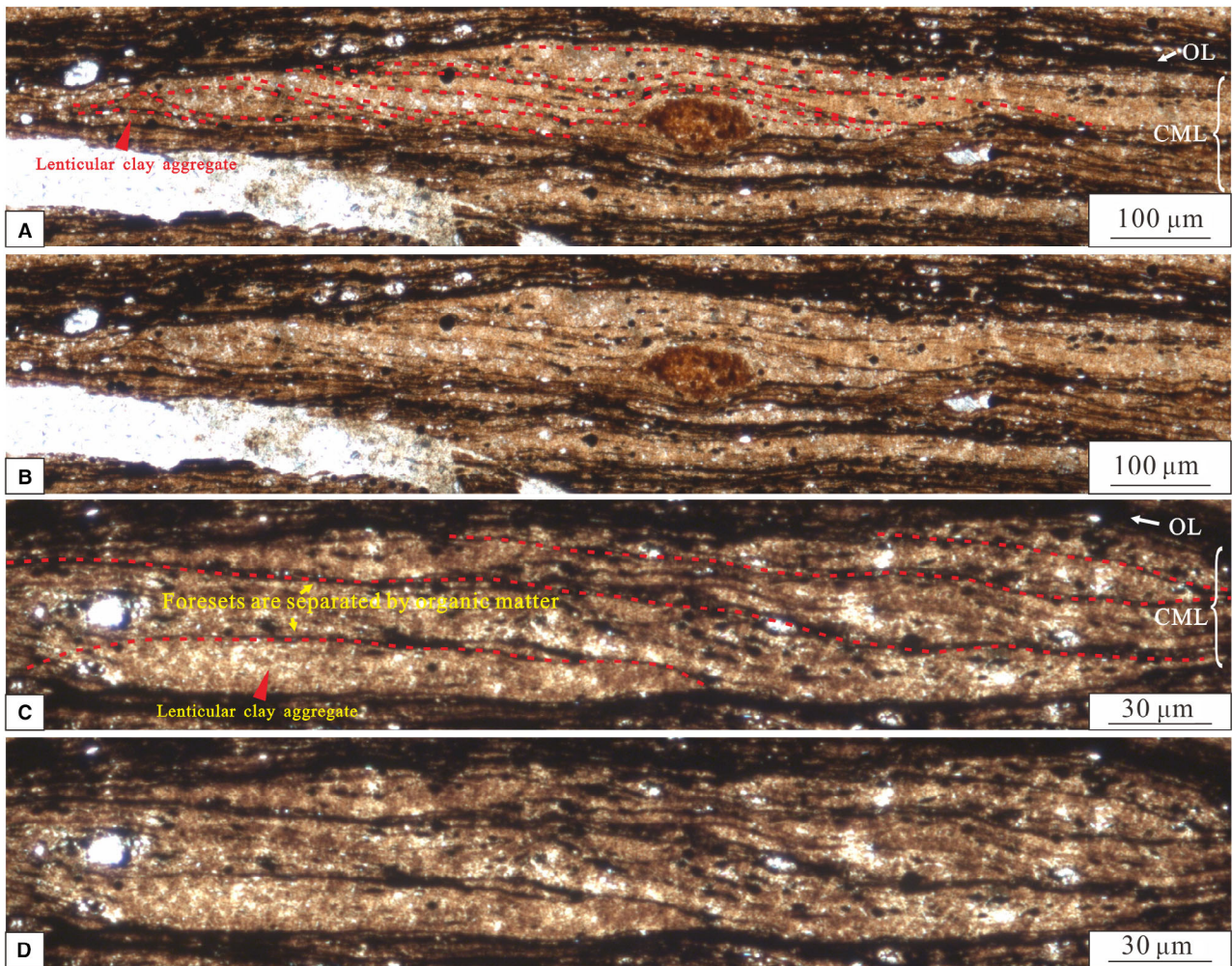
Fig. 8. Progradation features identified in the mud-grade sediments. (A) Multiple foresets can be discerned under polarized light, Well Ch96, 2057.35 m. (B) image taken from the same field of view as image (A), displaying the original characteristics of image (A) after removing the labels. (C) Lenticular clay aggregates can be identified under multiple foresets under polarized light, Well Ch96, 2055.55 m, the red arrow indicates the position of lenticular clay aggregates. (D) Image taken from the same field of view as image (C), displaying the original characteristics of image (C) after removing the labels. CML, clay mineral layer; OL, organic matter layer.

U can reach up to 48.36 ppm. Therefore, the analysis of logging data of a single well (Ch96) shows that the GR values of the deep-lacustrine shales are mainly higher than 300 API and can reach as high as 717.46 API (Fig. 11A). However, the GR values of the massive mudstone and sandstone can only reach 200 API and 150 API, respectively (Fig. 11A). In addition to the difference of GR values, there are also significant differences in mineral composition among shale, massive mudstones and sandstones (Zhang *et al.*, 2021b). This allows the authors to elucidate the correspondence between the logging data and the mineral composition by applying supervised machine learning, which is conducive to clarifying the spatial distribution of different lithofacies within the Ordos Basin (Zhang *et al.*, 2021b). Based on the analytical results of the logging data and supervised machine learning, this study found that F1 were deposited near the southern margin of the Ordos Basin and showed a relatively constant thinning towards the north (Fig. 11B). The provenance analysis just indicates that these mud-grade sediments with foresets and floccule ripples are mainly sourced by the volcaniclastic deposits from the
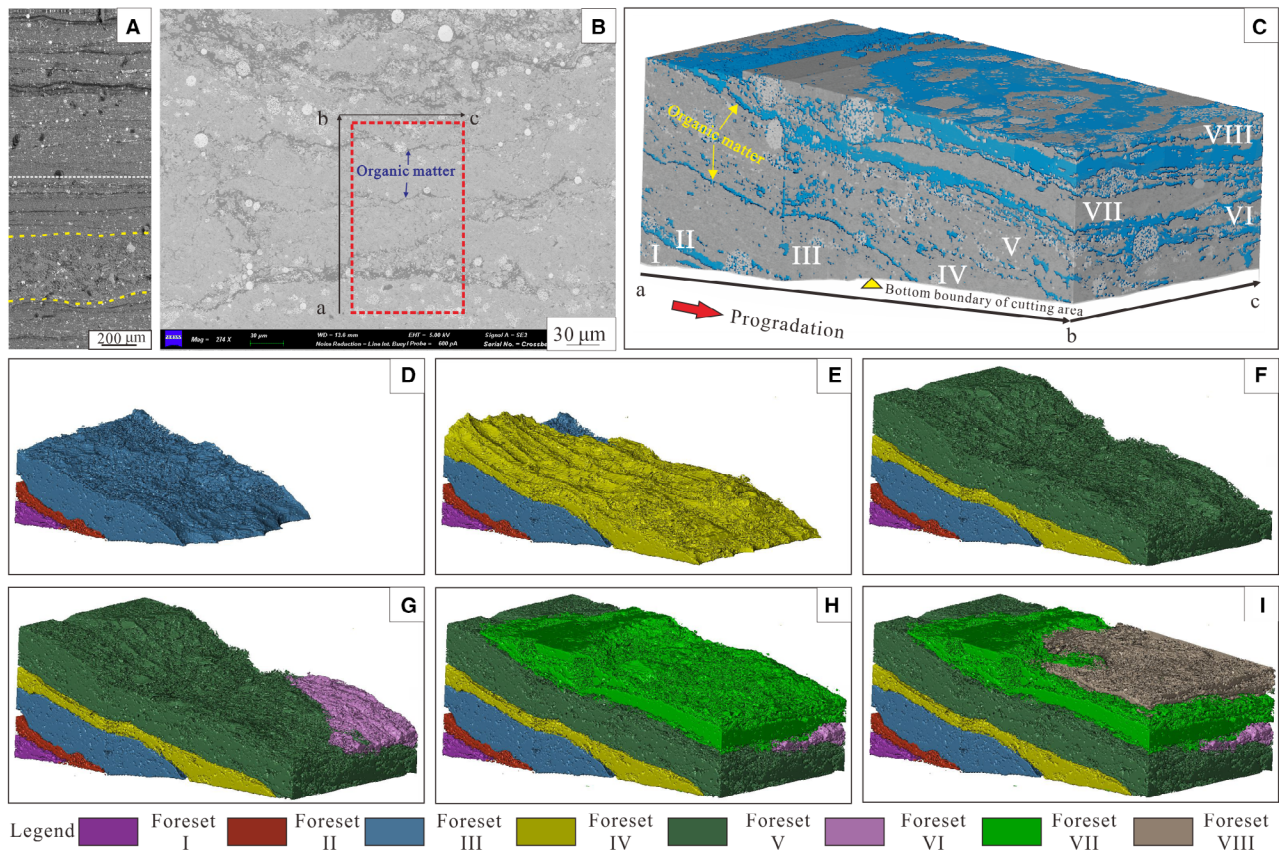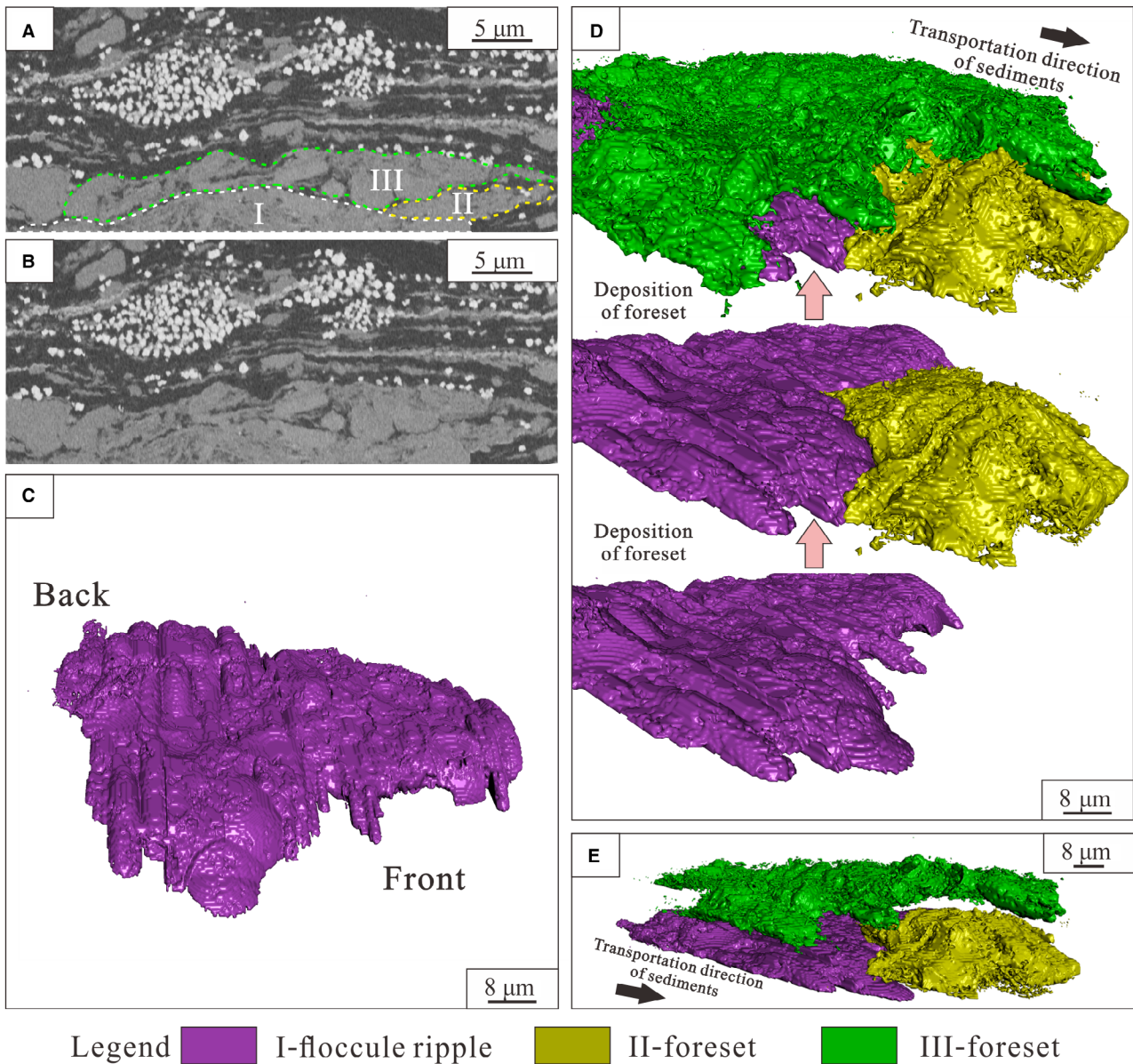
Fig. 9. Three-dimensional reconstruction of foresets in the mud-grade sediments. (A) Microscopic characteristics, Well Ch96, 2055.55 m, showing the silt-grade felsic lamina is located between two yellow dotted lines; when selecting typical areas for three dimensional reconstruction, the interface of silt-grade felsic laminae is used as the standard for cutting to ensure that the bottom boundary of the cutting area is parallel to the shale lamina (the white dashed line indicates that the cutting position is parallel to the silt-grade felsic lamina); since the interface of silt-grade felsic lamina can represent the horizontal interface during the deposition of mud-grade sediments, selecting cutting positions parallel to this lamina ensures that the bottom boundary of the cutting area is parallel to the sedimentary interface. (B) Cross-section of the cutting position shown in image (A) under SEM analysis, Well Ch96, 2055.55 m; (C) The three-dimensional reconstruction result on the basis of FIB-SEM (focused ion beam – scanning electron microscopy) analysis, the analysis area is within the red dashed box in image (B), and the numbers I to VIII refer to the different stages of foresets (from stages I to VIII); (D) to (H) display the spatial distribution of foresets during stages I to VIII; the foresets are generally separated by organic matter so that each stage of foreset can be extracted separately from the three-dimensional data set; a different colour was then assigned on different stages of foresets to facilitate differentiation.

Qingling orogenic belts in the southern part of the Ordos Basin (Lin *et al.*, 2024). On this basis, a cross-well profile of multiple wells from south to north was extracted. Combining with core observation and supervised machine learning, the authors determined the distribution of different lithofacies in each well within the profile (Fig. 12), which showed that the cumulative thickness ratio of F1 in Well N70 can reach up to 40%. At Well G292 to the north of N70, the cumulative thickness ratio of F1 can only reach 7.1% (Fig. 12), and F1 is completely unrecognizable at Well H234 (Fig. 12). This confirms that the proportion of F1 in sedimentary strata gradually decreases and eventually disappeared from south to north. Therefore, based on the provenance and spatial thickness variation of F1, the authors believe that the volcaniclastic materials from Qingling orogenic belts were transported mainly from south to north to provide the source for the deep-lacustrine mud-grade sediments.

Fig. 10. Three-dimensional characteristics of floccule ripples and their overlying foresets in the mud-grade sediments. (A) The lenticular clay aggregates for three-dimensional reconstruction analysis by FIB-SEM (focused ion beam – scanning electron microscopy; the cross-section perpendicular to the shale laminae), Well Ch96, 2062.3 m, the floccule ripple (I) and its overlying foresets (II and III) are marked in image (A). (B) Image taken from the same field of view as image (A), displaying the original characteristics of image (A) after removing the labels. (C) Three-dimensional characteristics of the floccule ripple (I) in image (A). (D) Three-dimensional characteristics of foresets (II and III) shown in image (A). (E) A side view of a floccule ripple (I) and its overlying foresets (II and III), with both foresets (II and III) shifted upward a certain distance to make the floccule ripple and foresets more visible.

DISCUSSION

Sedimentary origin of the deep-lacustrine mud-grade sediments

The identification of floc structures and foresets in the mud-grade sediments indicates that the deep-lacustrine setting of the Ordos Basin during deposition of the Chang 7_3 sub-member is not a continuously still water environment (Aplin & Macquaker, 2011; Tänavsuu-Milkeviciene & Frederick Sarg, 2012; Baas *et al.*, 2016). Therefore, suspension settling cannot adequately explain the depositional process of the mud-grade
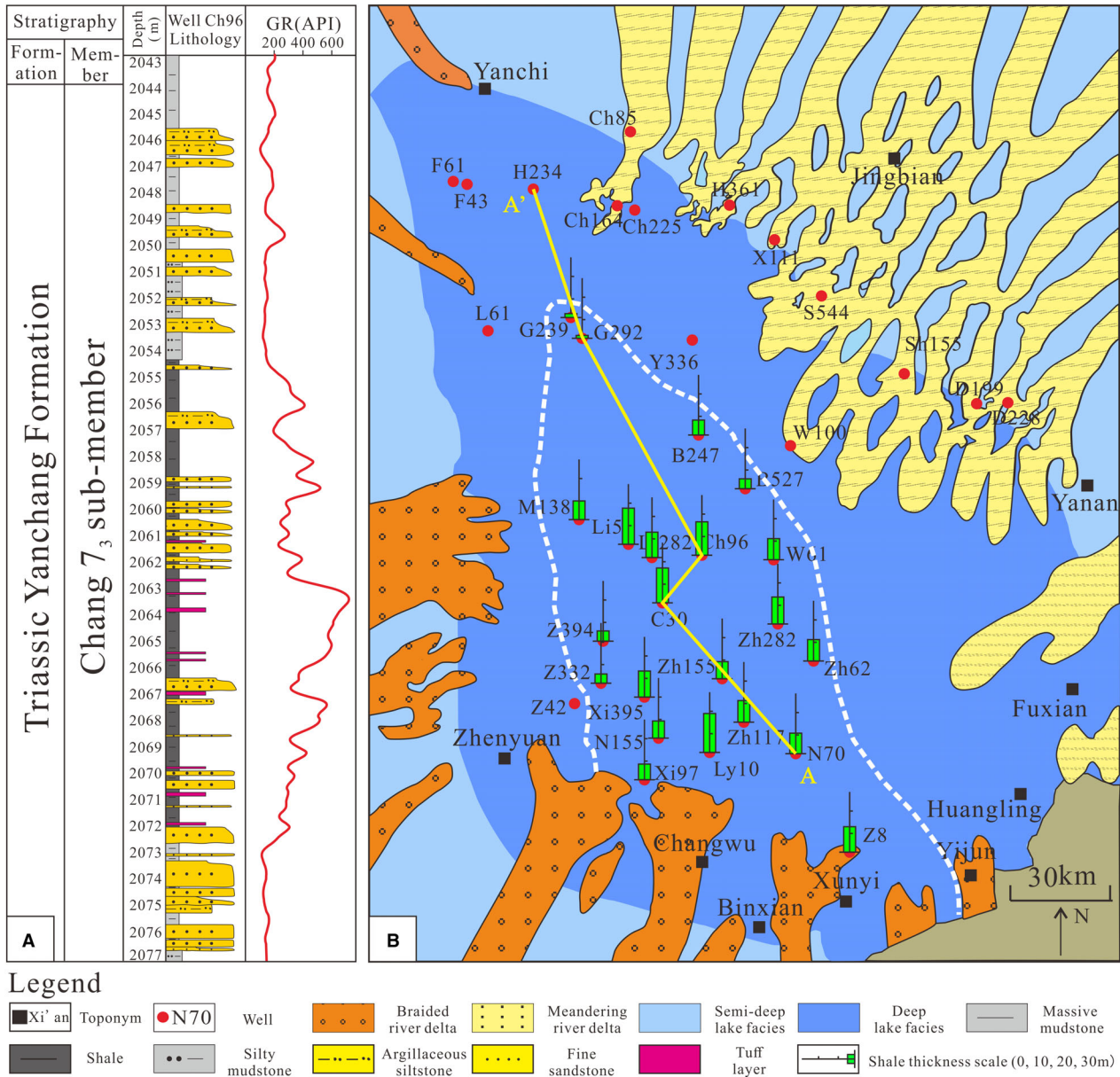
Fig. 11. Gamma ray (GR) logging data and the distribution of F1 within the Ordos Basin. The white dotted line denotes the known limits of the F1 distribution. The wells without a 'shale thickness scale' indicate that the thickness of F1 in that well is zero.

particles. The sedimentary origin of the mud-grade sediments in the deep-lacustrine setting needs to be further studied.

In freshwater lake basins, the abundant supply of volcaniclastic material can release many high-valence metal cations into the lake water (Frogner *et al.*, 2001; Duggen *et al.*, 2007) (Fig. 3A and B). The pH of the surface waters ranges from 7 to 9 (Singer *et al.*, 2002). Within this pH range, the surfaces of smectite, quartz and feldspar are negatively charged (Barclay & Worden, 2000; Zhang *et al.*, 2015). The high-valence metal cations therefore play an essential bridging role (Fig. 6A), promoting attraction and agglomeration of mud-grade feldspars and smectites by electrostatic forces (Fig. 6B and C) (Wang *et al.*, 2003; Gibbs & Hickey, 2018). However, the negative charges on the surfaces of clay minerals are typically
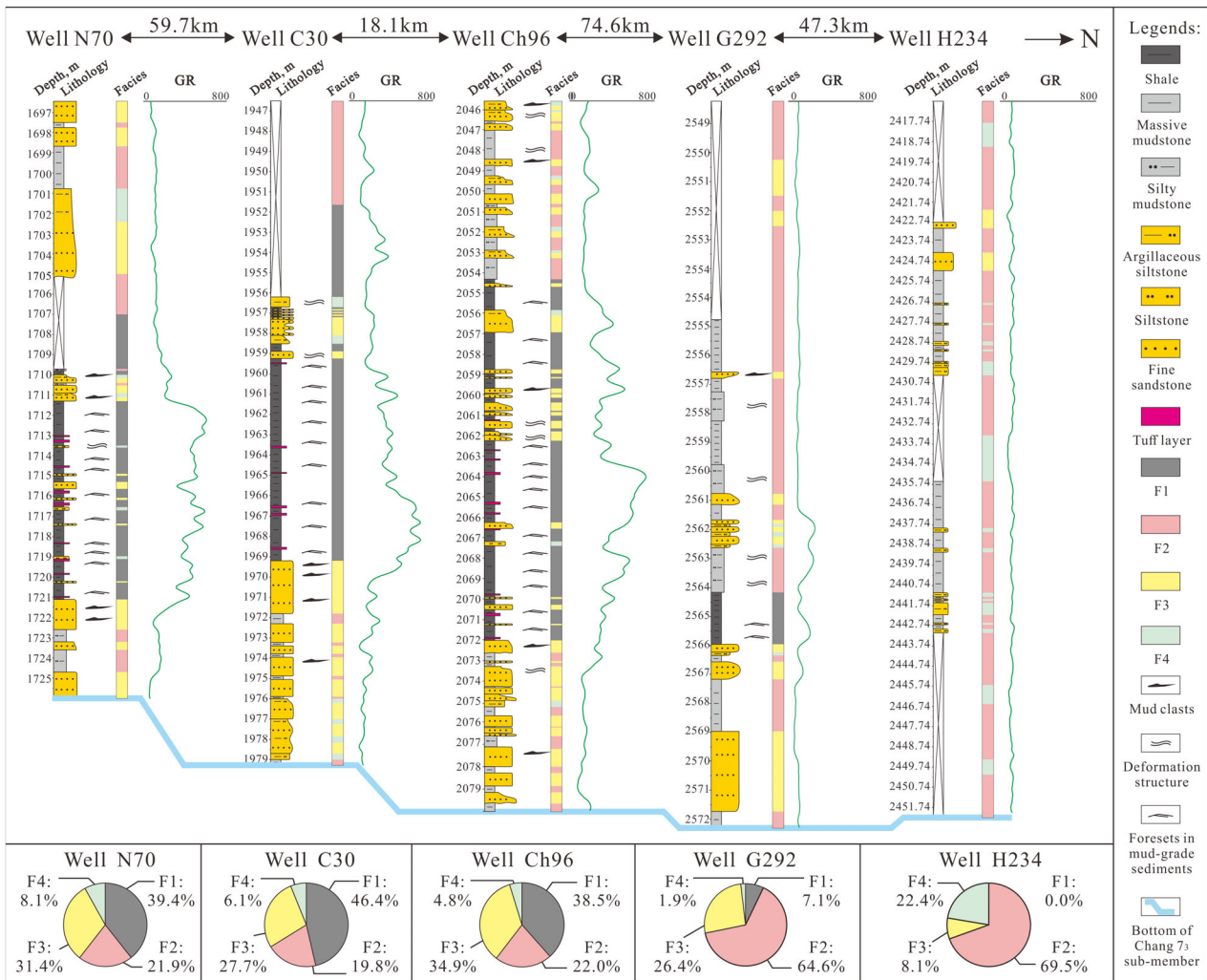
Fig. 12. Sedimentary logs of the Chang 7_3 sub-member and the cross-well profiles of multiple wells. The sedimentary logs of each well are from the Chang 7_3 sub-member of Triassic Yanchang Formation in the Ordos Basin. The locations of the wells in the cross-well profiles are distributed on line A–A' in Fig. 11B.

unevenly distributed. This usually shows as a positive charge at the edges of, or along defects in, the clay minerals, while typically appearing as a negative charge on the surface of clay minerals (Fig. 6A) (Bennett *et al.*, 1991). Therefore, electrostatic attraction can cause clay minerals to form flocs through 'edge–face' contact (Fig. 6B). Compared to single clay minerals, the flocs with particle sizes ranging from several microns to 1 mm have a faster settling rate (Fennessy *et al.*, 1994; Aplin & Macquaker, 2011); so they can easily and quickly settle onto the substrate (Schieber & Southard, 2009). Plint (2019) has clearly observed that the flocs composed of clay minerals can be transported in a flow rate of 0.08

to 0.12 m/s, which confirms that the flocs can move stably in the flow with a certain velocity without breaking. On this basis, multiple foresets and floccule ripples identified in the mud-grade sediments further indicate that, after settling onto the substrate, the flocs can undergo advective sediment transport processes at the sediment–water interface under the action of underflows.

There are many types of underflow capable of transporting clastic sediments, including debris flow, intrabasinal turbidity currents, contour currents, tidal flows and hyperpycnal flows (Stow *et al.*, 2001; Zuchuat *et al.*, 2019; Zavala, 2020). The debris-flow deposits are characterized by a homogeneous massive structure

and the significant column of clay matrix, along with the presence of outsized 'floating' skeletons and mudstone intraclasts (Yang *et al.*, 2017; Peng, 2021; Boulesteix *et al.*, 2022). However, this is different from the micro-sedimentary structures identified in the mud-grade sediments of the Ordos Basin (Figs 8 to 10). This indicates that the debris flow is not the primary underflow for transporting flocs in the deep-lacustrine setting. Intrabasinal turbidity current is a kind of underflow triggered mainly by volcanic eruption and earthquake (Yang *et al.*, 2015, 2017). It is difficult for these events to occur frequently and regularly on a scale of several decades. However, the time interval for the deposition of CML is approximately between two and eight years (Lin *et al.*, 2023). It is difficult to consider that the intrabasinal turbidity current is the dominant underflow for transporting mud-grade sediments in the Ordos Basin. Contour currents have the potential to move sediment along contours, oblique or parallel to the shoreline (DeReuil & Birgenheier, 2019). This leads to the deposition of contourites, which are mainly distributed as elongated drift bodies parallel to the shoreline, with a relatively limited extent in the direction perpendicular to the shoreline (Faugères *et al.*, 1999; Faugères & Stow, 2008). However, mud-grade sediments mainly develop near the southern margin of the Ordos Basin, and do not exhibit characteristics of distribution along the shoreline (Fig. 11B). Therefore, the flocs may not be transported mainly by the contour current in the Ordos Basin. Erosive-bases, flaser bedding, bi-directional ripple cross-lamination, abundant reactivation surfaces and wavy bedding can be identified in the sediments affected by tidal processes (Zuchuat *et al.*, 2019; El-Gendy *et al.*, 2022). Especially in the asymmetrical tide, the difference of flow velocity between high and low tide usually leads to the development of foresets and 'mud drapes' in the sediments (Allen, 1982). This is very similar to the distribution characteristics of the foresets and organic matter in the CML (Fig. 13A). In terms of flow types, the asymmetrical tidal flow seems to explain the origin of typical sedimentary structures in the mud-grade sediments of the Ordos Basin. Except for tidal flow, the steady advance of foresets may also record the unidirectional-current action (Fig. 13A) (Schieber & Southard, 2009). Hyperpycnal flow can transport fine-grained particles continuously to the centre of basin and form the sediments with multiple foresets (DeReuil & Birgenheier, 2019; Baker & Baas, 2020). *In situ* Raman spectral analysis proves that the terrigenous organic matter is indeed mixed within the CML (Fig. 13B). Therefore, hyperpycnal flow may also be an important flow type that induces the transport and deposition of flocs (Bhattacharya & MacEachern, 2009; Mulder & Chapron, 2011; DeReuil & Birgenheier, 2019).

The mud-grade sediments mainly deposited in the deep-lacustrine setting of the Ordos Basin, where they are likely protected from the effects of tidal action. Therefore, compared to the tidal flow, the authors are more inclined to define the underflow as hyperpycnal flow which induces the bedload transport of flocs in the deep-lacustrine setting. A previous study found that the humidity during the deposition of F1 was abnormally elevated compared to the period of F2 deposition (Lin *et al.*, 2024). The increase in humidity is usually reflected in the rainfall increase, which tends to trigger floods (Corella *et al.*, 2021). The frequent occurrence of floods also provides the possibility for the development of hyperpycnal flow in deep-lacustrine settings (Mulder *et al.*, 2003; Yang *et al.*, 2017; Dou *et al.*, 2019). During the process of bedload transport of flocs on the substrate, with the decrease of the velocity of hyperpycnal flow towards the centre of basin, the flocs with larger mass preferentially accumulate on the substrate. These deposits change the migration path of subsequent flocs, inducing part of the flocs to continuously accumulate along both sides of the earlier floc deposits to form floccule ripples. After that, some flocs can further cross the crest point of floccule ripples under the action of underflow, and then deposit on the ripple lee side, which forms multiple foresets that dip downstream (Plint, 2019). These processes lead to the lateral migration of foresets due to a continuous change in the shape of bedforms (Fig. 9E to I), which finally resulted in the stacking and lateral connection of many foresets as the front end of the foresets that continuously advanced forward (Schieber & Southard, 2009).

In deep-lacustrine settings, in addition to the floc sedimentation, organic matter deposition also occurs. Based on the microscopic observation, two occurrences of organic matter can be identified in the mud-grade sediments (Fig. 8), one is distributed between each foreset and floccule ripple, the other is in the form of organic matter within the layers themselves (Fig. 8). Although the actual sizes of the flocs cannot be quantitatively recovered, the floccule ripples of
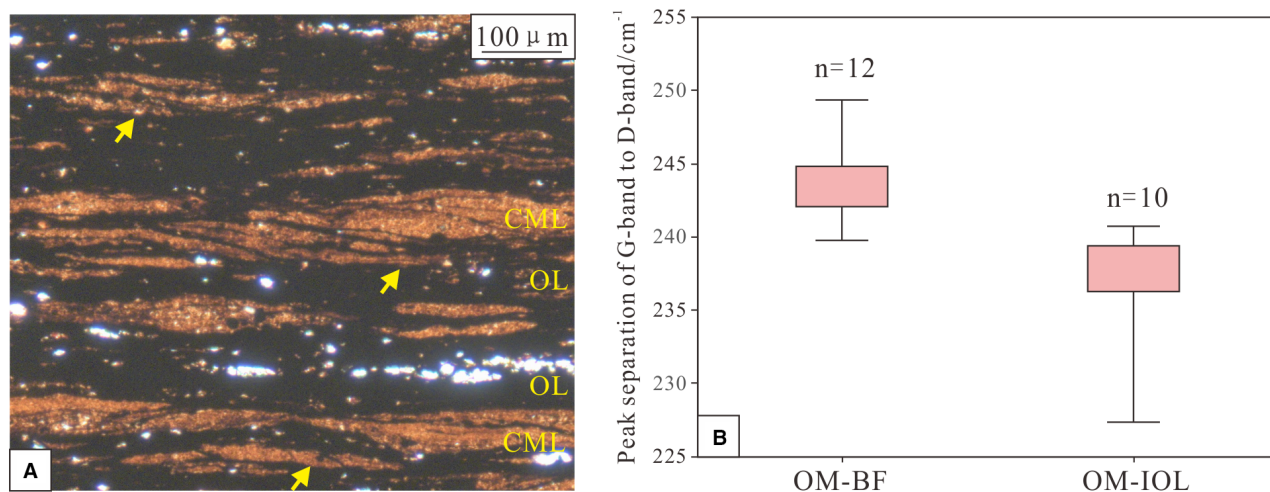
Fig. 13. Microscopic distribution characteristics of organic matter and the Raman parameters. (A) Microscopic distribution of organic matter in the mud-grade sediments. The organic layers are generally thicker than the organic matter between the foresets. The yellow arrows indicate the unidirectional foresets in different CML. (B) *In situ* laser Raman analysis on the organic matter with two occurrences. The peak separation of G-band and D-band is obviously higher in the organic matter between foresets (OM-BF) than that in the organic layers (OM-IOL), indicating that more benzene ring is included in the OM-BF than in the OM-IOL. The Raman analytical data derived from the same sample. The vertical distances of Raman test points in OM-BF and OM-IOL are less than 1 cm. According to the formula for calculating vitrinite reflectance (Ro) based on Raman parameters (Liu *et al.*, 2013), the Ro of OM-BF is about 0.5% higher than that of OM-IOL. Based on the average geothermal gradient of the Ordos Basin in the late Mesozoic (3.3 to 4.5°C/100 m) (Ren, 1996), under the condition of similar organic matter types, the 0.5% difference in Ro can only be realized when the variation in burial depth reaches about 500 m difference. However, the difference of vertical burial depths between OM-BF and OM-IOL are less than 1 cm. Such a small difference in burial depth does not cause significant changes in Ro, which proves that the difference in the content of benzene ring in organic matter is mainly caused by the supply of terrestrial organic matter. CML, clay mineral layer; OL, organic matter layer; OM-BF, organic matter between foresets; OM-IOL, organic matter in organic layers.

up to 40 μm in length were observed (Fig. 10). Because floccule ripples need to be formed by a large number of flocs (Schieber & South-ard, 2009), if the size of the flocs is 10 μm, the formation of the floccule ripple requires only four flocs, which seems impossible. Therefore, the authors speculate that the size of the flocs formed in the deep-lacustrine setting of the Ordos Basin should be much smaller than 10 μm. Observations of modern sediments show that the flocs with diameters of 1 to 10 μm are common (McCave, 1984). When the size of flocs is less than 10 μm, their density mainly ranges between 1.4 g/cm and 2.0 g/cm (McCave, 1984; Gibbs, 1985; Fennessy *et al.*, 1994), while the original density of kerogen mainly ranges between 1.0 g/cm and 1.4 g/cm (Stankiewicz *et al.*, 1994; Okiongbo *et al.*, 2005; Burn-ham, 2017). Therefore, in the deep-lacustrine setting of the Ordos Basin, the flocs settle more easily from the underflow onto the substrate than terrigenous organic matter (Ashley

et al., 1982; Bridge & Best, 1997). This may be an important reason for the general deposition of terrigenous organic matter on the top of each foreset within the CML (Figs 8 and 9). However, in the OL, contact features and distribution characteristics of the clay minerals have significant differences compared with those of the CML (Figs 5 and 7). The organic matter and clay minerals mainly occur as suspension settling in a still water environment to form OL (O'Brien *et al.*, 1980; Aplin & Macquaker, 2011). Therefore, the authors interpret that the CML, containing floccule ripples and foresets, were formed by bedload transport and deposition of flocs under the action of underflows. Since the hyperpycnal flow can carry oxygen to the deeper parts of the basin and temporarily reduce the reducibility of water column (Wilhelm *et al.*, 2016), this is not conducive to the effective preservation of organic matter. During the intermittent periods of underflow, due to lack of oxygen supply, the increased reducibility in the deep-lacustrine

setting was conducive to the preservation of organic matter, and this led to the development of OL.

Depositional model of the deep-lacustrine mud-grade sediments

A depositional model was further established in order to clearly describe the sedimentary process of mud-grade sediments in deep-lacustrine settings. During the transportation of mud-grade particles by hyperpycnal flow from south to north of the Ordos Basin, metal cations released by volcanoclastic materials promote flocculation under the action of electrostatic forces, forming numerous flocs within the underflow (Fig. 14A). Subsequently, the flocs gradually settle onto the substrate as the flow velocity decreased. The
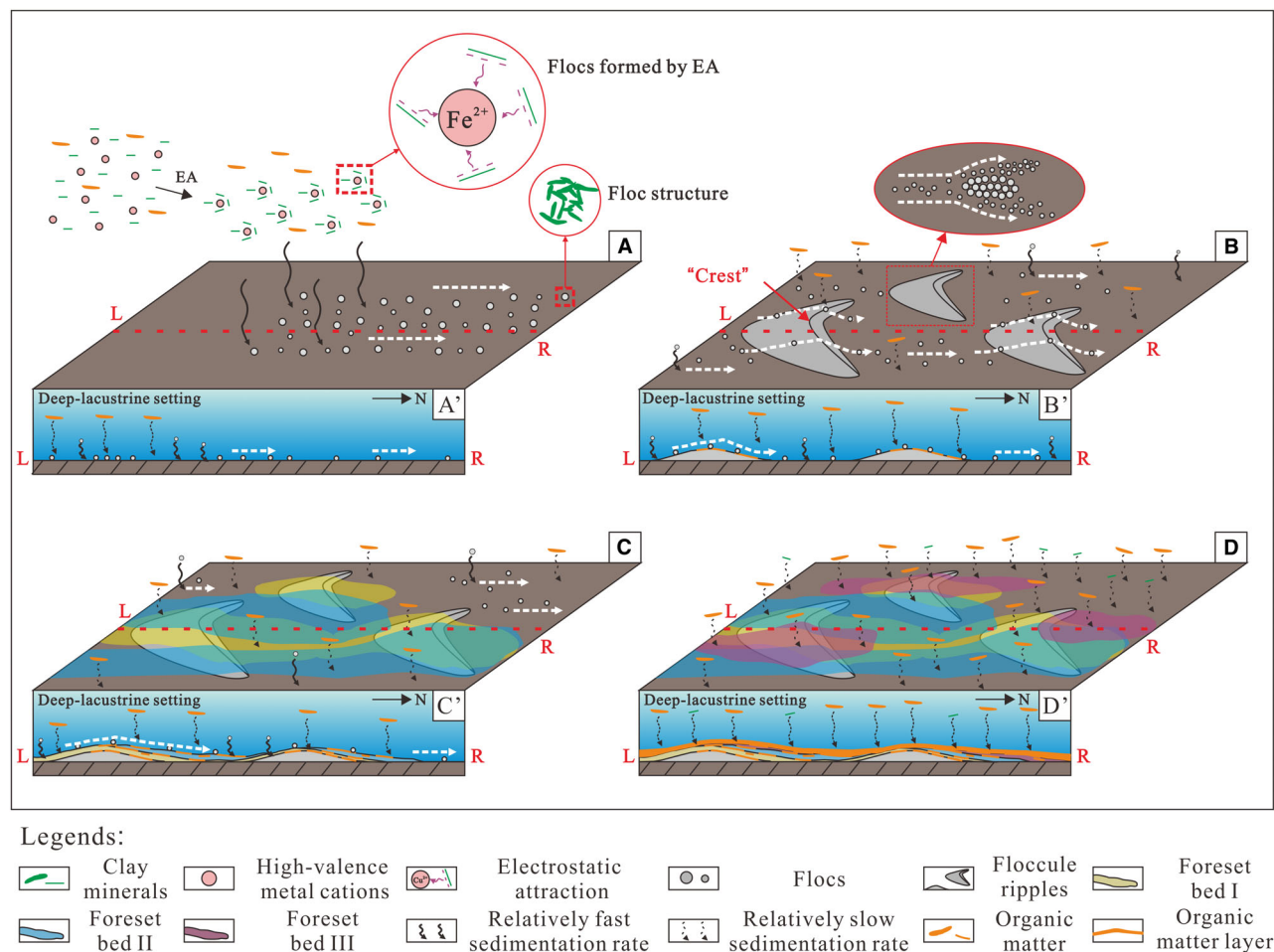
Fig. 14. Depositional process of mud-grade sediments in the deep-lacustrine setting of the Ordos Basin. (A) The input of volcaniclastic materials releases large amounts of high-valence metal cations, promoting flocculation of clay minerals under the action of electrostatic forces. After floc formation, as underflow velocity gradually decrease, the large amounts of flocs quickly settle onto the substrate, and then undergo bedload transport. (B) The continuous accumulation of flocs on the substrate induces the formation of floccule ripples. After that, the terrigenous organic matter within underflows slowly settles onto the surfaces of floccule ripples. (C) Multiple stages of foresets deposited on the lee sides of floccule ripples under the action of underflows. Multiple stages of foresets are stacked and laterally-connected, ultimately forming the clay mineral layer. The deposition of organic matter after each foreset formation makes it easy to distinguish the different foresets. (D) Continuous suspension settling of organic matter forming organic layers in the still-water environment during the intermittent period of underflows. The frequent development of hyperpycnal flow in the deep-lacustrine setting of the Ordos Basin leads to alternating deposition of organic matter layers and clay mineral layers, resulting in the formation of deep-lacustrine mud-grade sediments. The red dashed line in each image indicates the position of the cross-section. The continuous change in the shape of bedforms in the cross-section is actually caused by the deposition of floccule ripples and foresets. EA, electrostatic attraction; L, left side of the cross-section; R, right side of the cross-section.

flocs on the substrate will then occur as bedload transport under the action of underflow. Some flocs with larger mass preferentially terminate migration and accumulate on the substrate (Fig. 14B). These deposits hinder the bedload transport of subsequent flocs, forcing part of the flocs to accumulate along both sides of the earlier floc deposits and then form floccule ripples (Fig. 14B). After the formation of floccule ripples, the flocs can continue to migrate along their surfaces under the action of underflow and then accumulate on the lee side to develop multiple foresets (Fig. 14B). On the one hand, the continuous deposition of foresets causes their front end to advance forward downstream; on the other hand, the continuous change in the shape of bedforms also leads to the lateral migration of each foreset, which promotes lateral connection of multiple foresets, and finally forms CML (Fig. 14C). However, during the intermittent period of hyperpycnal flows, a relatively still-water environment occurs, and the sediment supply of the deep-lacustrine setting by underflows is limited. This low hydrodynamic condition also effectively reduces the contact probability of mud-grade particles, which prevents the formation of large flocs (Aplin & Macquaker, 2011). Clay minerals are mainly in the form of single particles and primarily occur as suspension settling, together with organic matter, to form OL (Fig. 14D).

CONCLUSIONS

This study first confirms that the floccule ripples and foresets can commonly be developed in the deep-lacustrine mud-grade sediments using the three-dimensional reconstruction analysis by focused ion beam – scanning electron microscopy (FIB-SEM). The mud-grade particles are not deposited only by suspension settling, underflow also has an important effect on the transport and deposition of mud-grade sediments in deep-lacustrine settings. Hyperpycnal flow is preliminarily considered as an important underflow for transporting mud-grade sediments. After the volcaniclastic materials are carried into the lake basin by hyperpycnal flows, a large number of metal cations are released, promoting the agglomeration of clay minerals to form flocs. As flow velocity decreased, the flocs settle continuously onto the substrate and then bedload transport occurs to form floccule ripples. After that, the subsequent flocs continually

cross the crest point and accumulate on the lee side of floccule ripples, inducing the front end of foresets to advance downstream and promoting the deposition of CML. During the intermittent period of underflows, the hydrodynamics in the deep-lacustrine setting is relatively weak, which limits floc formation. Clay minerals occur as suspension settling in the form of single particles along with organic matter, forming the organic matter layers between clay mineral layers.

DATA AVAILABILITY STATEMENT

Data will be made available on request.

REFERENCES

Alçiçek, H., Varol, B. and Özkul, M. (2007) Sedimentary facies, depositional environments and palaeogeographic evolution of the Neogene Denizli Basin, SW Anatolia, Turkey. *Sed. Geol.*, **202**, 596–637.

Allen, J.R.L. (1982) Mud drapes in sand-wave deposits: a physical model with application to the Folkestone Beds (early Cretaceous, southeast England). *Philosophical Transactions of the Royal Society of London*, **306**, 291–345.

Aplin, A.C. and Macquaker, J.H. (2011) Mudstone diversity: origin and implications for source, seal, and reservoir properties in petroleum systems. *AAPG Bull.*, **95**, 2031–2059.

Ashley, G.M., **Southard, J.B.** and **Boothroyd, J.C.** (1982) Deposition of climbing-ripple beds: a flume simulation. *Sedimentology*, **29**, 67–79.

Ayranci, K., **Harris, N.B.** and **Dong, T.** (2018) Sedimentological and ichnological characterization of the middle to upper Devonian Horn River Group, British Columbia, Canada: Insights Into Mudstone Depositional Conditions and Processes Below Storm Wave Base. *J. Sediment. Res.*, **88**, 1–23.

Barclay, S.A. and **Worden, R.H.** (2000) Effects of reservoir wettability on quartz cementation in oil fields. *Quartz Cementation Sandstones*, **29**, 103–117.

Baas, J.H., **Best, J.L.** and **Peakall, J.** (2011) Depositional processes, bedform development and hybrid bed formation in rapidly decelerated cohesive (mud–sand) sediment flows. *Sedimentology*, **58**, 1953–1987.

Baas, J.H., **Best, J.L.** and **Peakall, J.** (2016) Predicting bedforms and primary current stratification in cohesive mixtures of mud and sand. *Journal of the Geological Society*, **173**, 12–45.

Baker, M.L. and **Baas, J.H.** (2020) Mixed sand–mud bedforms produced by transient turbulent flows in the fringe of submarine fans: Indicators of flow transformation. *Sedimentology*, **67**, 2645–2671.

Bennett, R.H., **O'Brien, N.R.** and **Hulbert, M.H.** (1991) Determinants of clay and shale microfabric signatures: processes and mechanisms. In: *Microstructure of Fine-Grained Sediments*, pp. 5–32. Springer, New York, NY.

Bhattacharya, J.P. and **MacEachern, J.A.** (2009) Hyperpycnal rivers and prodeltaic shelves in the Cretaceous seaway of North America. *J. Sed. Res.*, **79**, 184–209.

Boulesteix, K., **Poyatos-Moré, M.**, **Flint, S.S.**, **Taylor, K.G.**, **Hodgson, D.M.** and **Hasiotis, S.T.** (2019) Transport and deposition of mud in deep-water environments: processes and stratigraphic implications. *Sedimentology*, **66**, 2894–2925.

Boulesteix, K., **Poyatos-Moré, M.**, **Flint, S.S.**, **Hodgson, D.M.**, **Taylor, K.G.** and **Parry, G.R.** (2020) Sedimentary facies and stratigraphic architecture of deep-water mudstones beyond the basin-floor fan sandstone pinchout. *J. Sediment. Res.*, **90**, 1678–1705.

Boulesteix, K., **Poyatos-Moré, M.**, **Flint, S.S.**, **Hodgson, D.M.**, **Taylor, K.T.** and **Brunt, R.L.** (2022) Sedimentologic and stratigraphic criteria to distinguish between basin-floor and slope mudstones: implications for the delivery of mud to deep-water environments. *Deposit. Rec.*, **8**, 958–988.

Bourget, J., **Zaragosi, S.**, **Ellouz-Zimmermann, S.**, **Ducassou, E.**, **Prins, M.A.**, **Garlan, T.**, **Lanfumey, V.**, **Schneider, J.L.**, **Rouillard, P.** and **Giraudeau, J.** (2010) Highstand vs. lowstand turbidite system growth in the Makran active margin: Imprints of high-frequency external controls on sediment delivery mechanisms to deep water systems. *Mar. Geol.*, **274**, 187–208.

Bridge, J. and **Best, J.I.M.** (1997) Preservation of planar laminae due to migration of low-relief bed waves over aggrading upper-stage plane beds: comparison of experimental data with theory. *Sedimentology*, **44**, 253–262.

Burnham, A.K. (2017) Porosity and permeability of Green River oil shale and their changes during retorting. *Fuel*, **203**, 208–213.

Burton, D., **Woolf, K.** and **Sullivan, B.** (2014) Lacustrine depositional environments in the Green River Formation, Uinta Basin: expression in outcrop and wireline logs. *AAPG Bull.*, **98**, 1699–1715.

Corella, J.P., **Benito, G.**, **Monteoliva, A.P.**, **Sigro, J.**, **Calle, M.**, **Valero-Garcés, B.L.**, **Stefanova, V.**, **Rico, E.**, **Favre, A.C.** and **Wilhelm, B.** (2021) A 1400-years flood frequency reconstruction for the Basque country (N Spain): integrating geological, historical and instrumental datasets. *Quatern. Sci. Rev.*, **262**, 106963.

Cuadros, J., **Caballero, E.**, **Huertas, F.J.**, **de Cisneros, C.J.**, **Huertas, F.** and **Linares, J.** (1999) Experimental alteration of volcanic tuff: smectite formation and effect on ^{18}O isotope composition. *Clays Clay Mineral.*, **47**, 769–776.

DeReuil, A.A. and **Birgenheier, L.P.** (2019) Sediment dispersal and organic carbon preservation in a dynamic mudstone-dominated system, Juana Lopez Member, Mancos Shale. *Sedimentology*, **66**, 1002–1041.

Dou, L., **Hou, J.**, **Song, S.**, **Zhang, L.**, **Liu, Y.**, **Sun, S.**, **Li, Y.**, **Wang, X.**, **Ren, X.**, **Tang, Y.**, **Tian, H.** and **Yang, Y.** (2019) Sedimentary characteristics of hyperpycnites in a shallow lacustrine environment: a case study from the Lower Cretaceous Xiguayuan Formation, Luanping Basin, Northeast China. *Geol. J.*, **55**, 3344–3360.

Duggen, S., **Croot, P.**, **Schacht, U.** and **Hoffmann, L.** (2007) Subduction zone volcanic ash can fertilize the surface ocean and stimulate phytoplankton growth: evidence from biogeochemical experiments and satellite data. *Geophys. Res. Lett.*, **34**, 1–5.

El-Gendy, N.H., **Radwan, A.E.**, **Waziry, M.A.**, **Dodd, T.J.H.** and **Barakat, M.K.** (2022) An integrated sedimentological, rock typing, image logs, and artificial neural networks analysis for reservoir quality assessment of the heterogeneous fluvial-deltaic Messinian Abu Madi reservoirs, Salma field, onshore East Nile Delta, Egypt. *Mar. Petrol. Geol.*, **145**, 105910.

Faugères, J.C. and **Stow, D.A.V.** (2008) Contourite drifts: nature, evolution and controls. *Dev. Sedimentol.*, **60**, 257–288.

Faugères, J.C., **Stow, D.A.**, **Imbert, P.** and **Viana, A.** (1999) Seismic features diagnostic of contourite drifts. *Mar. Geol.*, **162**(1), 1–38.

Fennessy, M.S., **Brueske, C.C.** and **Mitsch, W.J.** (1994) Sediment deposition patterns in restored freshwater wetlands using sediment traps. *Ecol. Eng.*, **3**, 409–428.

Fritz, W.J. and **Vanko, D.A.** (1992) Geochemistry and origin of a black mudstone in a volcaniclastic environment, Ordovician Lower Rhyolitic Tuff Formation, North Wales, UK. *Sedimentology*, **39**, 663–674.

Frogner, P., **Gíslason, S.R.** and **Oskarsson, N.** (2001) Fertilizing potential of volcanic ash in ocean surface water. *Geology*, **29**, 487–490.

Fu, J.H., **Li, S.X.**, **Xu, L.M.** and **Niu, X.B.** (2018) Paleo-sedimentary environmental restoration and its significance of Chang 7 Member of Triassic Yanchang Formation in Ordos Basin, NW China. *Petrol. Explor. Dev.*, **45**, 998–1008.

Fu, J.H., **Niu, X.B.**, **Dan, W.D.**, **Feng, S.B.**, **Liang, X.W.**, **Xin, H.G.** and **You, Y.** (2019) The geological characteristics and the progress on exploration and development of shale oil in Chang 7 Member of Mesozoic Yanchang Formation, Ordos Basin. *China Petrol. Explor.*, **24**, 601–614.

Fu, J.H., **Li, S.X.**, **Niu, X.B.**, **Deng, X.Q.** and **Zhou, X.P.** (2020) Geological characteristics and exploration of shale oil in Chang 7 Member of Triassic Yanchang Formation, Ordos Basin, NW China. *Petrol. Explor. Dev.*, **47**, 931–945.

Gibbs, R.J. (1985) Estuarine flocs: their size, settling velocity and density. *J. Geophys. Res. Oceans*, **90**(C2), 3249–3251.

Gibbs, M.M. and **Hickey, C.W.** (2018) Flocculants and sediment capping for phosphorus management. In: *Lake Restoration Handbook*, pp. 207–265. Springer, Cham.

Hayashi, K.I., **Fujisawa, H.**, **Holland, H.D.** and **Ohmoto, H.** (1997) Geochemistry of ∼1.9 Ga sedimentary rocks from northeastern Labrador, Canada. *Geochimica et Cosmochimica Acta*, **61**, 4115–4137.

Hou, L.H., **Pang, Z.L.**, **Luo, X.** and **Lin, S.H.** (2023) Sedimentary features of the gravity flow influenced shale deposit: a case study of Chang 7 member in the Ordos Basin, China. *Mar. Petrol. Geol.*, **153**, 106277.

Huff, W.D. (2016) K-bentonites: a review. *Am. Mineral.*, **101**, 43–70.

Jiang, Z.X., **Liang, C.**, **Wu, J.**, **Zhang, J.G.**, **Zhang, W.Z.**, **Wang, Y.S.**, **Liu, H.M.** and **Chen, X.** (2013) Several issues in sedimentological studies on hydrocarbon-bearing fine-grained sedimentary rocks. *Acta Petroloei Sinica*, **34**, 1031–1039.

Jin, Z.J., **Wang, G.P.**, **Liu, G.X.**, **Gao, B.**, **Liu, Q.Y.**, **Wang, H.L.**, **Liang, X.P.** and **Wang, R.Y.** (2021) Research progress and key scientific issues of continental shale oil in China. *Acta Pet. Sin.*, **42**, 821–835.

Könitzer, S.F., **Davies, S.J.**, **Stephenson, M.H.** and **Leng, M.J.** (2014) Depositional controls on mudstone lithofacies in a basinal setting: implications for the delivery of sedimentary organic matter. *J. Sediment. Res.*, **84**, 198–214.

Li, Y. and **Yang, R.C.** (2023) Astronomical calibration of a ten-million-year Triassic lacustrine record in the Ordos Basin, North China. *Sedimentology*, **70**, 407–433.

Li, W., **Liu, L.F.**, **Wang, Y.R.**, **Zhang, Z.H.** and **Lu, P.** (2012) Application of logging data in calculating mud shale thickness. *China Petrol. Explor.*, **17**, 32–35.

Li, Z.C., **Zhang, X.K.**, **Zeng, J.J.**, **Qi, J.H.**, **Zhang, H.F.** and **Yang, Z.Y.** (2019) The characteristics and geological significance of the Adakite rocks of the upper Triassic stata Huari formation volcanics in west Qinling. *Mineral Explor.*, **10**, 1361–1368.

Li, Z., **Schieber, J.** and **Pedersen, P.K.** (2021a) On the origin and significance of composite particles in mudstones: examples from the Cenomanian Dunvegan Formation. *Sedimentology*, **68**, 737–754.

Li, S.X., **Zhou, X.P.**, **Guo, Q.H.**, **Liu, J.P.**, **Liu, J.Y.**, **Li, S.T.**, **Wang, B.** and **Lyu, Q.Q.** (2021b) Research on evaluation method of movable hydrocarbon resources of shale oil in the Chang 7₃ sub-member in the Ordos Basin. *Nat. Gas Geosci.*, **32**, 1771–1784.

Liang, C., **Jiang, Z.**, **Cao, Y.**, **Wu, J.**, **Wang, Y.** and **Hao, F.** (2018) Sedimentary characteristics and origin of lacustrine organic-rich shales in the salinized Eocene Dongying Depression. *GSA Bull.*, **130**, 154–174.

Lin, M., **Xi, K.**, **Cao, Y.**, **Liu, K.** and **Zhu, R.** (2023) Periodic paleo-environment oscillation on multi-timescales in the Triassic and their significant implications for algal blooms: a case study on the lacustrine shales in Ordos Basin. *Palaeogeogr. Palaeoclimatol. Palaeoecol.*, **612**, 111376.

Lin, M.R., **Xi, K.L.**, **Cao, Y.C.**, **Niu, X.B.**, **Ma, W.J.**, **Wang, X.J.** and **Xu, S.** (2024) Palaeoenvironmental changes in the Late Triassic lacustrine facies of the Ordos Basin of Northwest China were driven by multistage volcanic activity: implications for the understanding the Carnian Pluvial Event. *Palaeogeogr. Palaeoclimatol. Palaeoecol.*, **637**, 112012.

Liu, Y.S., **Hu, Z.C.**, **Gao, S.**, **Günther, D.**, **Xu, J.**, **Gao, C.G.** and **Chen, H.H.** (2008) In situ analysis of major and trace elements of anhydrous minerals by LA-ICP-MS without applying an internal standard. *Chem. Geol.*, **257**, 34–43.

Liu, D.H., **Xiao, X.M.**, **Tian, H.**, **Min, Y.S.**, **Zhou, Q.**, **Cheng, P.** and **Shen, J.G.** (2013) Sample maturation calculated using Raman spectroscopic parameters for solid organics: methodology and geological applications. *China Sci. Bull.*, **58**, 1228–1241.

Liu, Q., **Yuan, X.J.**, **Lin, S.H.**, **Wang, L.**, **Guo, H.**, **Pan, S.Q.** and **Yao, J.L.** (2014) The classification of lacustrine mudrock and research on its' depositional environment. *Acta Sedimentol. Sinica*, **32**, 1016–1025.

Liu, B.C., **Li, K.N.**, **Shi, H.L.**, **Pu, W.F.**, **Wang, H.T.** and **Wang, S.H.** (2018) Petrogenesis and tectonic implications of late Triassic volcanic rocks at the Gansu-Qinghai junction in the west Qinling mountains. *Geoscience*, **32**, 704–717.

Liu, X.Y., **Li, S.X.**, **Guo, Q.H.**, **Zhou, X.P.** and **Liu, J.Y.** (2021) Characteristics of rock types and exploration significance of the shale strata in the Chang 7₃ sub-member of Yanchang Formation, Ordos Basin, Chine. *Nat. Gas Geosci.*, **32**, 1177–1189.

Loucks, R.G. and **Ruppel, S.C.** (2007) Mississippian Barnett Shale: lithofacies and depositional setting of a deep-water shale-gas succession in the Fort Worth Basin, Texas. *AAPG Bull.*, **91**, 579–601.

Macquaker, J.H.S., **Bentley, S.J.** and **Bohacs, K.M.** (2010) Wave-enhanced sediment-gravity flows and mud dispersal across continental shelves: reappraising sediment transport processes operating in ancient mudstone successions. *Geology*, **38**, 947–950.

Mángano, M.G., **Buatois, L.A.**, **Wu, X.**, **Sun, J.** and **Zhang, G.** (1994) Sedimentary facies, depositional processes and climatic controls in a Triassic lake, Tanzhuang Formation, western Henan Province, China. *J. Paleolimnol.*, **11**, 41–65.

McCave, I.N. (1984) Size spectra and aggregation of suspended particles in the deep ocean. *Deep Sea Res. Part A. Oceanogr. Res. Pap.*, **31**, 329–352.

Mulder, T. and **Chapron, E.** (2011) Flood deposits in continental and marine environments: character and significance.

Mulder, T., **Syvitski, J.P.**, **Migeon, S.**, **Faugères, J.C.** and **Savoye, B.** (2003) Marine hyperpycnal flows: initiation, behavior and related deposits. A review. *Mar. Petrol. Geol.*, **20**, 861–882.

O'Brien, N.R. (1996) Shale lamination and sedimentary processes. *Geol. Soc. Lond. Spec. Publ.*, **116**, 23–36.

O'Brien, N.R., **Nakazawa, K.** and **Tokuhashi, S.** (1980) Use of clay fabric to distinguish turbiditic and hemipelagic siltstones and silts. *Sedimentology*, **27**, 47–61.

Okiongbo, K.S., **Aplin, A.C.** and **Larter, S.R.** (2005) Changes in type II kerogen density as a function of maturity: evidence from the kimmeridge clay formation. *Energy Fuel*, **19**, 2495–2499.

Peng, J. (2021) Sedimentology of the upper Pennsylvanian organic-rich Cline Shale, Midland Basin: from gravity flows to pelagic suspension fallout. *Sedimentology*, **68**, 805–833.

Plint, A.G. (2014) Mud dispersal across a Cretaceous prodelta: storm-generated, wave-enhanced sediment gravity flows inferred from mudstone microtexture and microfacies. *Sedimentology*, **61**, 609–647.

Plint, A.G. (2019) Mud bedforms in a natural ice flume. *Sed. Rec.*, **17**, 4–7.

Ren, Z.L. (1996) Research on the relations between geothermal history and oil-gas accumulation in the Ordos Basin. *Acta Pet. Sin.*, **17**, 17–24.

Schieber, J. (1991) *Sedimentary Structures: Textures and Depositional Settings of Shales from the Lower Belt*

Supergroup, Mid-Proterozoic, Montana, USA//Microstructure of Fine-Grained Sediments, pp. 101–108. Springer, New York, NY.

Schieber, J. (2011) Reverse engineering mother nature-shale sedimentology from an experimental perspective. *Sed. Geol.*, **238**, 1–22.

Schieber, J. and **Southard, J.B.** (2009) Bedload transport of mud by floccule ripples-direct observation of ripple migration processes and their implications. *Geology*, **37**, 483–486.

Schieber, J. and **Yawar, Z.** (2009) A new twist on mud deposition-mud ripples in experiment and rock record. *Sed. Rec.*, **7**, 4–8.

Schieber, J., **Southard, J.** and **Thaisen, K.** (2007) Accretion of mudstone beds from migrating floccule ripples. *Science*, **318**, 1760–1763.

Schieber, J., **Southard, J.B.** and **Schimmelmann, A.** (2010) Lenticular shale fabrics resulting from intermittent erosion of water-rich muds-interpreting the rock record in the light of recent flume experiments. *J. Sediment. Res.*, **80**, 119–128.

Singer, H., **Müller, S.**, **Tixier, C.** and **Pillonel, L.** (2002) Triclosan: occurrence and fate of a widely used biocide in the aquatic environment: field measurements in wastewater treatment plants, surface waters, and lake sediments. *Environ. Sci. Technol.*, **36**, 4998–5004.

Slatt, R.M. and **O'Brien, N.R.** (2011) Pore types in the Barnett and Woodford gas shales: contribution to understanding gas storage and migration pathways in fine-grained rocks. *AAPG Bull.*, **95**, 2017–2030.

Stankiewicz, B.A., **Kruge, M.A.** and **Crelling, J.C.** (1994) Density gradient centrifugation: application to the separation of maceráis of type I, II, and III sedimentary organic matter. *Energy Fuel*, **8**, 1513–1521.

Stow, D.A.V. and **Piper, D.J.W.** (1984) Deep-water fine-grained sediments: facies models. *Geol. Soc. Lond. Spec. Publ.*, **15**, 611–646.

Stow, D.A.V. and **Shanmugam, G.** (1980) Sequence of structures in fine-grained turbidites: comparison of recent deep-sea and ancient flysch sediments. *Sed. Geol.*, **25**, 23–42.

Stow, D.A.V., **Huc, A.Y.** and **Bertrand, P.** (2001) Depositional processes of black shales in deep water. *Mar. Petrol. Geol.*, **18**, 491–498.

Tänavsuu-Milkeviciene, K. and **Frederick Sarg, J.** (2012) Evolution of an organic-rich lake basin-stratigraphy, climate and tectonics: Piceance Creek basin, Eocene Green River Formation. *Sedimentology*, **59**, 1735–1768.

Taylor, S.R. and **McLennan, S.M.** (1995) The geochemical evolution of the continental crust. *Rev. Geophys.*, **33**, 241–265.

Tombo, S.L., **Dennielou, B.**, **Berne, S.**, **Bassetti, M.A.**, **Toucanne, S.**, **Jorry, S.J.**, **Jouet, G.** and **Fontanier, C.** (2015) Sea-level control on turbidite activity in the Rhone canyon and the upper fan during the Last Glacial Maximum and Early deglacial. *Sed. Geol.*, **323**, 148–166.

Wang, Y.L., **Li, D.P.** and **Xie, M.S.** (2003) Research and advance in flocculation morphology. *Techniques Equipment Environ. Pollut. Control*, **10**, 1–9.

Wang, F., **Chen, R.**, **Yu, W.**, **Tian, J.**, **Liang, X.**, **Tan, X.** and **Gong, L.** (2021) Characteristics of lacustrine deepwater fine-grained lithofacies and source-reservoir combination of tight oil in the Triassic Chang 7 member in Ordos Basin, China. *J. Pet. Sci. Eng.*, **202**, 108429.

Wang, R.G., **Li, W.H.**, **Liao, Y.Y.**, **Guo, Y.Q.** and **Liu, H.W.** (2013) Provenance analysis of Chang 7 Member of Triassic Yanchang Formation in Ordos Basin. *Geological Bulletin of China*, **32**, 671–684.

Wilhelm, B., **Bogel, H.**, **Crouzet, C.**, **Etienne, D.** and **Anselmetti, F.S.** (2016) Frequency and intensity of palaeofloods at the interface of Atlantic and Mediterranean climate domains. *Clim. Past*, **12**, 299–316.

Wilson, R.D. and **Schieber, J.** (2014) Muddy prodeltaic hyperpycnites in the lower Genesee Group of central New York, USA: implications for mud transport in epicontinental seas. *J. Sediment. Res.*, **84**, 866–874.

Yang, T., **Cao, Y.C.**, **Wang, Y.Z.**, **Li, Y.** and **Zhang, S.M.** (2015) Status and trends in research on deep-water gravity flow deposits. *Acta Geol. Sin.*, **89**, 610–631.

Yang, H., **Niu, X.B.**, **Xu, L.M.**, **Feng, S.B.**, **You, Y.**, **Liang, X.W.**, **Wang, F.** and **Zhan, D.D.** (2016) Exploration potential of shale oil in Chang7 Member, Upper Triassic Yanchang Formation, Ordos Basin, NW China. *Petrol. Explor. Dev.*, **43**, 511–520.

Yang, R., **Jin, Z.**, **van Loon, A.T.**, **Han, Z.** and **Fan, A.** (2017) Climatic and tectonic controls of lacustrine hyperpycnite origination in the Late Triassic Ordos Basin, central China: implications for unconventional petroleum development. *AAPG Bull.*, **101**, 95–117.

Yuan, X.J., **Lin, S.H.**, **Liu, Q.**, **Yao, J.L.**, **Wang, L.**, **Guo, H.**, **Deng, X.Q.** and **Cheng, D.W.** (2015) Lacustrine fine-grained sedimentary features and organic-rich shale distribution pattern: a case study of Chang 7 Member of Triassic Yanchang Formation in Ordos Basin, NW China. *Petrol. Explor. Dev.*, **42**, 37–47.

Zavala, C. (2020) Hyperpycnal (over density) flows and deposits. *J. Palaeogeogr.*, **9**, 1–21.

Zhang, C.L., **Zhang, L.**, **Chen, T.S.**, **Zhang, Y.**, **Yang, Y.J.**, **Huang, J.**, **He, J.** and **Li, H.** (2013) Provenance and parent-rock types of member 7 of Yanchang Formation (Triassic), Ordos Basin. *Acta Sedimentol. Sinica*, **31**, 430–439.

Zhang, L., **Lu, X.**, **Liu, X.**, **Yang, K.** and **Zhou, H.** (2015) Surface wettability of basal surfaces of clay minerals: insights from molecular dynamics simulation. *Energy Fuel*, **30**, 149–160.

Zhang, W.Z., **Yang, H.**, **Xia, X.Y.**, **Xie, L.Q.** and **Xie, G.W.** (2016) Triassic chrysophyte cyst fossils discovered in the Ordos Basin, China. *Geology*, **44**, 1031–1034.

Zhang, J.Q., **Li, S.X.**, **Zhou, X.P.**, **Liu, J.Y.**, **Guo, R.L.**, **Chen, J.L.** and **Li, S.T.** (2021a) Gravity flow deposits in the distal lacustrine basin of the 7th reservoir group of Yanchang Formation and deepwater oil and gas exploration in Ordos Basin: a case study of Chang 7_3 sublayer of Chengye horizontal well region. *Acta Pet. Sin.*, **42**, 570–587.

Zhang, Y.Y., **Xi, K.L.**, **Cao, Y.C.**, **Yu, B.H.**, **Wang, H.**, **Lin, M.R.**, **Li, K.** and **Zhang, Y.Y.** (2021b) The application of machine learning under supervision in identification of shale lamina combination types-A case study of Chang 73 sub-member organic-rich shales in the Triassic Yanchang Formation, Ordos Basin, NW China. *Petrol. Sci.*, **18**, 1619–1629.

Zhao, W.Z., **Zhu, R.K.**, **Hu, S.Y.**, **Hou, L.H.** and **Wu, S.T.** (2020) Accumulation contribution differences between lacustrine organic-rich shales and mudstones and their significance in shale oil evaluation. *Petrol. Explor. Dev.*, **47**, 1160–1171.

Zhou, D.W., **Zhao, C.Y.**, **Li, Y.D.**, **Jian, W.C.**, **Ye, J.** and **Chen, G.** (1995) *Geological Features of Southwest Margin of Ordos Basin and its Relationships with Qinling Orogenic Belt*. Geological Publishing House, Beijing. 4 pp.

Zhu, X.M., **Ji, H.C.** and **Xie, Q.B.** (2008) *Sedimentary Petrology*. Petroleum Industry Publishing House, Beijing. 54 pp.

Zhu, R.K., **Li, M.Y.**, **Yang, J.R.**, **Zhang, S.R.**, **Cai, Y.**, **Cao, Y.** and **Kang, Y.** (2022) Advances and trends of fine-grained sedimentology. *Oil Gas Geol.*, **43**, 251–264.

Zou, C.N., **Qiu, Z.**, **Zhang, J.Q.**, **Li, Z.Y.**, **Wei, H.Y.**, **Liu, B.**, **Zhao, J.H.**, **Yang, T.**, **Zhu, S.F.**, **Tao, H.F.**, **Zhang, F.Y.**, **Wang, Y.M.**, **Zhang, Q.**, **Liu, W.**, **Liu, H.L.**, **Feng, Z.Q.**, **Liu, D.**, **Gao, J.L.**, **Liu, R.** and **Li, Y.F.** (2022) Unconventional petroleum sedimentology: a key to understanding unconventional hydrocarbon accumulation. *Engineering*, **18**, 62–78.

Zuchuat, V., **Sleveland, A.R.N.**, **Pettigrew, R.P.**, **Dodd, T.J.H.**, **Clarke, S.M.**, **Rabbel, O.**, **Braathen, A.** and **Midtkanda, I.** (2019) Overprinted allocyclic processes by tidal resonance in an epicontinental basin: The Upper Jurassic Curtis Formation, east-central Utah, USA. *Depositional Rec.*, **5**, 272–305.